Native Silicon Oxide Properties Determined by Doping

Native Silicon Oxide Properties Determined by Doping

Michele Della Ciana[a,†], Alessandro Kovtun[b], Caterina Summonte[c], Andrea Candini[b], Daniela Cavalcoli[d], Denis Gentili[a], Roberta Nipoti[c] and Cristiano Albonetti[a]*

a. Consiglio Nazionale delle Ricerche - Istituto per lo Studio dei Materiali Nanostrutturati (CNR-ISMN) via P. Gobetti 101, 40129 Bologna, Italy

b. Consiglio Nazionale delle Ricerche - Istituto per la Sintesi Organica e la Fotoreattività (CNR-ISOF) via P. Gobetti 101, 40129 Bologna, Italy

c. Consiglio Nazionale delle Ricerche - Istituto per la Microelettronica e Microsistemi (CNR-IMM) via P. Gobetti 101, 40129 Bologna, Italy

d. Department of Physics and Astronomy, University of Bologna, Viale Berti Pichat 6/2, 40127, Bologna, Italy

KEYWORDS: native silicon oxide, doping concentration, contact angle, surface energy, surface chemistry.

ABSTRACT: The chemical-physical properties of native oxide layers, spontaneously forming on crystalline Si wafers, can be strictly correlated to the dopant type and the doping level. In particular, our investigations have focused on oxide layers forming upon air exposure in a clean room after Si wafer production, for doping concentration levels from ≈ 10^{13} to ≈ 10^{19} cm^{-3}. In order to determine these correlations, we have studied the surface, the bulk, and its interface with Si. The surface is investigated with contact angle, thermal desorption and atomic force microscopy obtaining information on the surface energy, cleanliness, and morphology, respectively. The thickness is measured with Ellipsometry and the chemical composition with X-ray Photoemission Spectroscopy. The electrostatic charges within the oxide layer and at the interface with Si are studied with Kelvin Probe Microscopy. We find that some properties show an abrupt change, i.e. thickness, while others present a maximum, i.e. silanol concentration and Si intermediate-oxidation states, at a critical doping concentration of ≈ $2.1 \cdot 10^{15}$ cm^{-3}. Additionally, two electrostatic contributions originate from the silanols present on the surface and the net charge distributed within the layer. Lastly, the surface roughness also depends on the doping concentration, showing a minimum at the same critical doping concentration. These findings can be fully reproduced for oxide layers re-grown in a clean room after a chemical etching of the native ones.

1. INTRODUCTION

It is widely believed that the chemical-physical properties of native silicon oxides (n-SiO_x), i.e. spontaneously formed upon exposure to clean room air after wafer production (also known as unintentional silicon oxide), cannot be controlled and therefore is irreproducible. This conviction probably arises from microelectronic manufacturing, where n-SiO_x was discarded as an ultra-thin dielectric layer because of its low breakdown voltage[1] and recurring current leakages,[2] and thus systematically removed in order to produce ultraclean Si surfaces for the fabrication of electronic devices.[3] This opinion has become popular with time in other scientific fields and it has been only partially studied. Consequently, the literature is not abundant and scattered over a period of fifty years.

Morita and co-workers[4] have systemically studied n-SiO_x, explaining the time evolution of its growth, measuring the thickness and resolving its chemical composition with X-ray photoemission spectroscopy (XPS). The doping of the crystalline Si, type (*n*- or *p*-) and concentration *N*, was mentioned as possibly correlated to the chemical and physical properties of the n-SiO_x but not deeply investigated. A direct correlation between *N* and the chemical composition of n-SiO_x was found by Ying *et al.*,[5,6] but their works are limited to crystalline and polycrystalline *n*-type Si substrates, lightly (*N* ≈ $8 \cdot 10^{14}$ cm^{-3}) and heavily (*N* ≈ $1 \cdot 10^{20}$ cm^{-3}) doped. To the best of our knowledge, Wolkenberg's work[7] is the sole example of a systematic investigation of n-SiO_x for different doping types and increasing concentrations, spanning over six order of magnitude. The author identified oxide defects as responsible for the chemical and physical properties of the n-SiO_x versus doping, however experiments and theory do not fit together.

To investigate such inconsistency, this work examines in depth the chemical and physical properties of n-SiO_x grown on crystalline Si substrates, doped with different types of dopants and with an increasing doping concentration from ≈ 10^{13} to ≈ 10^{19} cm^{-3}. Our investigations have focused solely on n-SiO_x grown in a clean room after wafer production ("as received") or regrown in a clean room after removal of the pristine layer.

A complete picture of n-SiO_x vs. *N* and dopant type can be obtained investigating the samples from the surface to the n-SiO_x/Si interface. The surface was investigated in terms of: (i) surface energy with Contact Angle measurements; (ii) surface cleanliness using Thermal desorption (TD); and (iii) surface morphology with Atomic Force Microscopy (AFM). Then, the bulk was investigated in terms of thickness (iv) and chemical composition (v) by means of Ellipsometry and XPS, respectively. Finally, the electrostatic charges at the n-SiO_x/Si interface (vi) were studied with Kelvin Probe (KP).

2. EXPERIMENTAL AND METHODS

2.1 Silicon wafers The experiments were performed on commercial polished Si wafers with a diameter of 10 cm (4-inch) and a thickness of (525±25) μm. The wafers were produced by different companies (e.g. Sil'tronix-France, Siltronic-Germany) in different periods, using either the Czochralski (CZ) or the floating zone (FZ) methods. Each wafer has a different resistivity ρ (in Ω·cm), i.e. a different doping concentration N (in cm^{-3}), obtained by incorporating a dopant (*viz*. B, P or As) in Si during the semiconductor ingot growth. All wafers have the same crystal orientation (100).

Table 1. List of the silicon wafers[a]

n°	Dopant	-type	ρ (Ω·cm)	N (cm^{-3})
1	As	n	< 0.0015	$(6.2\pm0.3)\cdot10^{19}$
2	B	p	< 0.005	$(2.1\pm0.1)\cdot10^{19}$
3	P	n	0.07-1	$(7.3\pm6.8)\cdot10^{16}$
4	B	p	0.1-0.5	$(1.4\pm1.1)\cdot10^{17}$
5	B	p	0.8-1.2	$(1.6\pm0.3)\cdot10^{16}$
6	B	p	1-5	$(1.0\pm0.7)\cdot10^{16}$
7	P	n	1-10	$(3\pm2)\cdot10^{15}$
8	B	p	1-10	$(9\pm8)\cdot10^{15}$
9	B	p	2-10	$(4\pm3)\cdot10^{15}$
10	B	p	5-10	$(2.1\pm0.7)\cdot10^{15}$
11	P	n	5-10	$(7\pm2)\cdot10^{14}$
12	P	n	7	$(6.5\pm0.1)\cdot10^{14}$
13	B	p	10-12	$(1.4\pm0.1)\cdot10^{15}$
14	B	p	14-22	$(8\pm2)\cdot10^{14}$
15	B	p	140-360	$(7.3\pm3.2)\cdot10^{13}$
16	B	p	500-1000	$(2.0\pm0.7)\cdot10^{13}$

[a] Progressive number of wafers, dopants, and consequent extrinsic Si type, i.e. *n*- or *p*-type. The resistivity range ρ measured and reported by producers considers the changes of ρ overall the wafer surface.[8] Such resistivity ranges are then converted into average doping concentration N by using an online calculator (last column).[9] In particular, N was calculated averaging the doping concentration of the extremes, i.e. their sum divided by 2, while the absolute error reported in the last column is the half of their difference. For wafers with not precise (wafers 1 and 2) or precise (wafer 12) resistivity, N is fixed to the converted ρ value, e.g. 0.0015 Ω·cm corresponds to $6.2\cdot10^{19}$ cm^{-3}, whereas their absolute errors are calculated from specific relative errors reported in the literature,[10] i.e. 4% and 1% for not precise and precise resistivity, respectively.

2.2 Storage The silicon wafers were singularly stored in plastic carrier trays to avoid any possible electrostatic charge effect caused by storing conditions in wafer cassettes.[11] This precaution reduces greatly the organic matter accumulated on the wafer surface, that results minimal and morphologically invisible.[12] The carrier trays were then stored in an archiving box inside a closet and, as a standard procedure, they were opened only under a vertical laminar flow hood for the time strictly necessary to prepare the samples. This procedure grants a minimal particle contamination, consisting of a single or, at most, few nanometric objects, ≈ 10 nm high and ≈ 100 nm wide, on a 30 × 30 μm^2 area.

2.3 Sample preparation The samples were prepared manually cleaving the wafers in ≈ 1×1 cm^2 chips.[13] To avoid Si powder contamination, the wafer polished surfaces are placed face-down on a clean science precision wipe during the cleaving procedure (Kimtech, Kimberly-Clark's, Dallas, TX, USA). Lastly, the sample is cleaned with acetone vapors to remove physical or chemical contaminants.[14,15]

2.4 Contact angle measurements The surface energies were measured through the method proposed by Owens and Wendt (O-W),[16] from contact angles of different characterization liquids measured with the sessile drop technique (Contact Angle Meter, GBX Scientific LTD, Ireland). The contact angle θ (in rad) of a liquid drop on a solid surface is related to the energies (in $dyn\cdot cm^{-1}$) of the liquid-vapor surface (γ_{LV}), solid surface-vapor (γ_{SV}), and the solid-liquid interface (γ_{SL}) according to the Young equation:

$$\gamma_{SV} = \gamma_{SL} + \gamma_{LV}\cos\theta \qquad (1)$$

In general, the surface energy γ is due to polar (dipole-dipole and dipole-induced dipole) and dispersive (induced dipole-induced dipole) forces at the surface. As described by Fowkes,[17] the surface energy of a liquid and a solid can be written as a sum of their polar (γ^p) and dispersive force (γ^d) components ($\gamma = \gamma^p + \gamma^d$). Based upon this additivity, the O-W model proposes the following semi-empirical formula to calculate γ_{SL}:[16]

$$\gamma_{SL} = \gamma_{SV} + \gamma_{LV} - 2\left(\sqrt{\gamma_S^d\gamma_L^d} + \sqrt{\gamma_S^p\gamma_L^p}\right) \qquad (2)$$

Combining the Equations 1 and 2, one obtains the following linear relation:

$$\gamma_{LV}(1+\cos\theta) = 2\left(\sqrt{\gamma_S^d\gamma_L^d} + \sqrt{\gamma_S^p\gamma_L^p}\right) \qquad (3)$$

Since γ_{SV} has to be found, Equation 3 is divided by $(\gamma_L^d)^{1/2}$:

$$\frac{\gamma_{LV}(1+\cos\theta)}{2\sqrt{\gamma_L^d}} = \sqrt{\gamma_S^d} + \sqrt{\gamma_S^p}\sqrt{\frac{\gamma_L^p}{\gamma_L^d}} \qquad (4)$$

that, with respect to the liquid drop (γ_{LV}, γ_L^d and γ_L^p), is a straight line:

$$y = x\sqrt{\gamma_S^p} + \sqrt{\gamma_S^d} \;\Rightarrow\; y = \frac{(1+\cos\theta)\gamma_{LV}}{2\sqrt{\gamma_L^d}}, x = \sqrt{\frac{\gamma_L^p}{\gamma_L^d}} \qquad (5)$$

The liquids employed (through their polar, γ_L^p, and dispersive, γ_L^d components) and their correspondent θ determine the x and y values. Following the Equation 5, the polar (γ_S^p) and dispersive (γ_S^d) components of the sample surface can be obtained from the slope and the y-intercept of the data linear fit. The O-W model assumes a negligible surface pressure π_{SV} (also known as spreading pressure, same units of the surface tension),[18] which is an additional pressure arising from the molecules adsorbed on the surface that, in some cases, can affect the contact angle measurements.

By definition, $\pi_{SV} = \gamma_S - \gamma_{SV}$ where γ_S is the surface energy of a solid surface in vacuum,[18] which is the sample energy. In the case of contact angle measurements performed in air, the amount of adsorbed molecules, mainly water, depends on the Relative Humidity (RH) and the temperature (T_A) of the

environment. In our operational conditions (RH ≈ 40%, T_A = 26°C), the adsorption isotherm plot for water molecules adsorbed on amorphous silica (that is similar to the n-SiO_x) reports an amount of absorbed water molecules in the range of 1-2 µmol·m^{-2},[19] corresponding to a negligible π_{SV} of a few dyn·cm^{-1}.[20]

Although the O-W model is unable to discern the origin of the surface forces, it is a simple method to evaluate the polar and dispersive components of the solid surface that provides experimental results comparable to those obtained with more sophisticated models.[21] The use of the O-W model is suitable for a moderately polar surface[22] like the n-SiO_x that is expected to be a substrate chemically inert[23,24] or, at most, weakly interacting.[25]

On the basis of availability in laboratory,[26,27] high surface energy bipolar liquids, i.e. deionized water, glycerol, ethylene glycol and dimethylformamide, were chosen for having the largest possible range of liquid surface energies ($\gamma_{LV} = \gamma_L$, see Table 2). The correspondent polar (γ_L^p), and dispersive force (γ_L^d) components of these liquids, hence their γ_L, were obtained averaging the values taken from the literature[28–35] with the standard deviation as the absolute error.[36]

Table 2. Liquid energy values[b]

Liquid	γ_L (dyn·cm^{-1})	γ_L^p (dyn·cm^{-1})	γ_L^d (dyn·cm^{-1})
water	72.8±0.1	50.8±0.4	22.0±0.3
glycerol	63.6±0.3	28±2	35.8±1.6
ethylene glycol	48.2±0.4	17.9±1.4	30.4±1.8
dimethyl-formamide	37±1	7.7±0.4	29.1±1.4

[b] Characterization liquids with decreasing total energies γ_L and the correspondent polar γ_L^p and dispersive force γ_L^d components. Values and errors were obtained averaging those from the literature. The range of liquid energies γ_L is consistent with the range adopted for common contact angle measurements.[37]

The contact angle measurements were performed on wafers 1, 3, 5, 8, 9, 10, 12, 13, 14 and 16 (see Table 1). The measured θ for each liquid represents the average of three θ values in three different sample regions (see Supplementary Materials). Prior to contact angle measurements, samples were cleaned with a solvent-cleaning process.[38] The samples were washed in acetone, isopropanol, and deionized water with steps of 5 min each, and, finally, they were dried with a pure nitrogen stream. As proved by repeated contact angle measurements on the same sample,[36] the initial θ is restored after the solvent-cleaning process. Such solvent-cleaning process is able to remove most of contaminants adsorbed on the n-SiO_x surface.[39]

The contact angle hysteresis H helps to better characterize the n-SiO_x surfaces. Measuring advancing θ_a and receding θ_r contact angles is more meaningful than a static, metastable angle θ, somewhere in between θ_a and θ_r.[40] The Young's equation (Equation 1) applied to a specific liquid-solid system determines a unique (static) contact angle θ for the three unique thermodynamic parameters γ_{LV}, γ_{SV} and γ_{SL} If the three-phase contact line moves when expanding (adding liquid) and contracting the liquid drop (removing liquid), θ changes becoming "dynamic". In the expanding (contracting) process, θ reaches an equilibrium angle θ_a (θ_r).[41]

These angles are the minimum, θ_r, and the maximum, θ_a, of an angle interval depending on both the liquid and the surface. The difference between θ_a and θ_r normalized with respect to θ_a is the dimensionless reduced hysteresis H,[42] i.e. $H = (\theta_a - \theta_r)\cdot \theta_a^{-1}$, which mainly depends on the roughness and/or the chemical heterogeneity of the surface.[43,44] The hysteresis experiments were performed only with deionized water (relatively nonvolatile) because of H yielded a unique value for each surface, independently of the contact liquid used.[45] During the experiments, the drop volume may vary from 1 (removing liquid stage) to 7 µl (adding liquid stage) in ≈ 12 s and θ is measured each ≈ 300 ms to follow its dynamics. These experimental conditions are comparable with the literature.[45]

2.5 Thermal desorption measurements The thermal desorption (TD) measurements were performed in vacuum (base pressure 1·10^{-8} mbar). To obtain an initial chemically clean surface, the sample was sonicated in acetone (15 min), 2-propanol (15 min), treated with piranha solution (H_2SO_4/H_2O_2, 3/1 v/v, 15 min) (Caution: preparation of the piranha solution is highly exothermic and reacts violently with organics), rinsed with DI water, and finally baked in air at 120°C for 15 min. To reproduce an amount of airborne contaminants comparable to the storage life of the other samples, the sample was then stored for 14 months in a plastic carrier tray (cp. Section 2.2).

As reported in the literature,[46,47] a temperature T_S of ≈ 450 °C permits a complete desorption of the airborne contaminants from the silicon oxide surface. The sample was mechanically fixed with metal clamps on the sample holder and heated up to 450°C using the Joule effect with a power of 14 W. As monitored by a K-type thermocouple, the maximum T_S was reached with a heating rate of ≈ 8°C/min. The amount of desorbed molecules was measured with a Residual Gas Analyser (RGA) composed of a triple-filter quadrupole (HAL/3F 301 RC, Hiden, UK) and equipped with a Faraday Cup detector.

2.6 Functional groups on the n-SiO_x surfaces The main functional groups present on n-SiO_x surfaces are siloxane bridges (Si–O–Si) and hydroxyl groups (Si–OH),[48] and both can be responsible for θ changes.[49,50] In particular, the Si–O–Si functional group promote surface polar interactions due to their structural arrangements,[51] polar interactions that are responsible for unintentional physical and chemical adsorption of airborne contaminants.[52] Conversely, such polarity can exploited to adsorb intentionally silane molecules on the n-SiO_x surface in both solution or vapor.[53,54] Silane molecules adsorbed on the n-SiO_x surface form a Self-Assembly Monolayer (SAM) whose surface coverage Θ (in percentage) is correlated to the surface density of the –OH groups. From this perspective, silane molecules act as a "probe molecule" that visualize the spatial distribution of the –OH groups on the sample surface.[55]

Tridecafluoro-1,1,2,2-tetrahydrooctyl-1-trichlorosilane (TFOCS, Sigma-Aldrich, purity 97 %, used without further purification) was deposited from a vapor phase on the substrate evaporating pure molecules under vacuum (≈ 1

mBar, obtained by using a vacuum membrane pump without gas purging. The experimental protocol and the vacuum system are equal to the ones reported in Ref. [56]). Before any treatment with TFOCS, the n-SiO_x samples were sonicated in acetone (15 min), 2-propanol (15 min) and water (15 min), and then baked at 120°C in air (15 min). This solvent-cleaning process removes most of the airborne contaminants usually covering the n-SiO_x surface exposed to air.[57] Then, the n-SiO_x samples were exposed to TFOCS vapor atmosphere at room temperature for 30 min in a vacuum desiccator. Prior to characterization, the substrates were aged under low-vacuum conditions for at least 24 hours. The functionalization experiments were performed on wafers 1, 5, 7, and 14 (see Table 1). The SAMs were imaged with Scanning Electron Microscopy (SEM-FEG HITACHI 4000, Japan).

2.7 Morphology of the n-SiO_x samples The topographic images of the n-SiO_x surfaces were collected with an AFM (SOLVER HV-MFM, NT-MDT Zelenograd, Moscow, RU) operating in intermittent contact, using HA_NC cantilevers (NT-MDT, Cantilever A: ω_0 = (235 ± 10) kHz and k = (12 ± 2) N·m^{-1}, Cantilever B: ω_0 = (140 ± 10) kHz and k = (3.5 ± 0.7) N·m^{-1}). Surface imaging was performed in air with operational conditions of RH = (71 ± 15) % and T_A ≈ 25°C. The imaged area was fixed to 1 μm x 1 μm, a size that permits to appreciate different nanometric features at smaller and larger length-scales.[58] The morphological evolution of the n-SiO_x vs. N can be described by the roughness σ,[59] and the Height-Height Correlation Function (HHCF)[60] (see Supplementary Materials). The morphological measurements were performed on wafers 1, 3, 5, 7, 8, 9, 10, 11, 12, 13, 14 and 16 (see Table 1).

2.8 Ellipsometric measurements of the n-SiO_x thicknesses The n-SiO_x thickness, t, was measured in air by analyzing ψ-Δ parameters obtained by using a Spectroscopy Ellipsometer (SE, MM-16, Horiba Jobin Yvon, Kyoto, Japan) with a fixed angle of incidence of 55°.

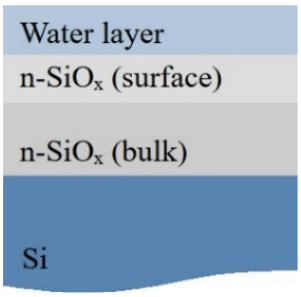

Figure 1. n-SiO_x model adopted to simulate experimental ellipsometric spectra.

Although ultrathin Si oxide was studied for several years,[61–64] evaluating its thickness from SE measurements is not trivial. Several issues concerning the interfacial layer near the Si substrate make it hard to model the n-SiO_x. Such interfacial layer consists of few atomic layers containing Si atoms in intermediate oxidation states, i.e., Si_20, SiO, and Si_20_3, and it occupies ≈ 50 % of the whole n-SiO_x thickness,[65] whereas the remaining ≈ 50 % is occupied by an over layer composed solely of SiO_2.[65–68] The spatial distribution of each intermediate oxidation state is still unknown (in particular with respect to the doping concentration N), thus making hard determine the refractive index of each intermediate oxidation layer[61–63] and their mutual correlations.[62] The surface roughness and the water layer adsorbed on the n-SiO_x surface due to RH,[64,69–71] affect as well SE measurements. Furthermore, SE measurements of ultrathin layer are less sensitive to ψ,[71] so experimental data are virtually limited to Δ. Solve some of such issues is out the scope of this paper, however they are useful to set up a model of the n-SiO_x as (see Figure 1): i) a water layer absorbed on the n-SiO_x surface, assumed to be conformal to the surface roughness and ≈ 0.4 nm thick (about 2 monolayers of water at RH ≈ 65 %);[72,73] ii) a layer to model the n-SiO_x surface and its roughness, as measured by AFM (see Section 2.7). As mentioned above, it is composed solely of SiO_2; iii) a layer to model the n-SiO_x bulk; and iv) the Si substrate. Layers ii) and iii) are described by the Bruggeman Effective Medium Approximation (BEMA).[74]

Since ellispometric measurements are performed in the same day and within few hours, the water layer thickness can be considered constant to ≈ 0.4 nm for all samples. The thickness of the n-SiO_x (surface) layer is determined by the average roughness σ of the sample surface measured by AFM that is obtained by averaging horizontal topographic profiles.[75] By approximating the average topographic profile to a sinusoidal trace, σ is the average oscillation amplitude with respect to the mean level height.[76] Accordingly, the thickness of the n-SiO_x (surface) layer is 2·σ and, due to periodic oscillations, it is composed of the 50 % of voids and the 50 % of SiO_2. This composition for rough surface is commonly adopted in SE simulations (see Table 3).[77] In view of interfacial layer issues, the thickness of the n-SiO_x (bulk) layer is unknown and left free in simulations. Its composition is modelled as two consecutive half-spaces: the upper one is made of SiO_2, the lower one as a silicon rich SiO_x oxide, which in turn can be optically modelled by an effective medium composed by SiO_2 and Si with equal volume fractions.[62,65] An alternative composition has been used for the n-SiO_x sample with the lowest N (fractions reported within brackets in Table 3).

Table 3. Composition of layers modelling n-SiO_x[c]

Layer	Composition	Thickness
water	H_2O – 100%	0.4 nm
n-SiO_x (surface)	SiO_2 – 50 %, Voids – 50 %	AFM
n-SiO_x (bulk)	SiO_2 – 75%; Si - 25 % (Si – 25 %, SiO_2 – 25 %, Voids – 50 %)	calculated from simulations
Si substrate	Si – 100%	Semi-infinite

[c] Layers and their BEMA fractional compositions adopted to model n-SiO_x samples. For Si and SiO_2, optical data useful for interpreting experimental results were taken from Palik's book.[78] Water and voids have n = 1.33, k = 0 and n = 1, k = 0, respectively. Fractions in brackets are used solely for the n-SiO_x sample with lowest N.

Within BEMA approximation, simulated data based on the model of Figure 1are expected to match experimental data within a margin of error of ± 10 %.[79] Calculated thicknesses of n-SiO_x samples are obtained by fitting ψ-Δ spectra with

the method of minimum χ^2 estimation. The ellipsometric measurements were performed on wafers 1, 3, 5, 7, 9, 10, 12, 13, 14 and 16 (see Table 1).

2.9 X-ray photoemission spectroscopy measurements X-ray photoemission spectroscopy (XPS) was performed with an ultrahigh vacuum (UHV) apparatus (base pressure 2×10^{-8} mbar) using a non-monochromatic Mg Kα excitation source (1253.6 eV, XR-50, Specs) with a constant power of 125 W and a hemispherical energy analyzer (Phoibos 100, Specs, Germany). The XPS experiments were performed on wafers 1, 3, 5, 10, 14 and 16 (see Table 1). The n-SiO_x samples were fixed on a sample holder with a conductive carbon tape, that is also electrically grounded. The photoelectrons coming from the sample were collected along the direction normal to the surface on an area of 7 × 3 mm^2, as selected by the XPS analyzer. All the spectra were calibrated with respect to the position of C 1s, corresponding to 285.0 eV. The Shirley background was subtracted, and fitting of the Si 2p peaks was performed using the CasaXPS software.[80]

2.10 Kelvin probe measurements The work function (WF, in V) was measured employing macroscopic Kelvin Probe (KP), performed under ambient conditions using a 2 mm diameter gold tip amplifier (Ambient Kelvin Probe KP020 from KP Technology Ltd., Wick, UK). The WF measurements were performed at a fixed probe-sample position (mean distance ≈ 0.5 mm) by applying two DC voltages (- 7 and 7 V) to a mechanically oscillating probe (frequency in the range 50 – 80 Hz).[81] The sample WF is obtained by averaging measured potentials for approximately two minutes.

For each measured sample, we probed at least four different locations using the average and deviation as the mean value and corresponding error (as the minimum error value was set 0.01 eV). The KP measurements were performed on wafers 1, 2, 3, 4, 5, 6, 7, 8, 10, 11, 13, 14, 15 and 16 (see Table 1). The wafers 2, 4, 14 and 15 were specifically added to the KP measurements to complete some missing doping concentration. Before and after each measurement, the probe calibration was done using as a reference a freshly cleaved Highly Oriented Pyrolytic Graphite (WF = 4.65 V).

Airborne contaminants on the n-SiO_x surface,[82] T and RH[83] can affect the KP measurements. To obtain reproducible and comparable results the samples were cleaned with the procedure described in Section 2.5 and stored in a low vacuum (≈ 1 mbar) for 6 months. Then, they were exposed to air for a week to stabilize the surface with the same amount of surface contaminants and all the wafers were measured consecutively in the same session of measurements to keep constant T_A (22 °C) and RH (≈ 55 %). Temperature changes of few Celsius degrees do not affect KP measurements[84] whilst an appreciable change of the WF vs. RH is observable only after the 70 %.[85]

3. RESULTS

3.1 Surface energy of the n-SiO_x samples and their polar and dispersive components As shown in Figure 2a, the surface energy γ_S of the n-SiO_x samples depends on both doping types (squares for *p*-type and dots for *n*-type) and the doping concentration N from ≈ 10^{13} to ≈ 10^{19} cm^{-3}. In particular, *p*-type samples doped with B show a strong dependence of γ_S vs. N, presenting a peak in the range [$5\cdot10^{14}$; $4\cdot10^{15}$] cm^{-3} with a maximum of ≈ 50 dyn·cm^{-1} for N ≈ $2.1\cdot10^{15}$ cm^{-3} and a baseline of (19±8) dyn·cm^{-1}. *n*-type samples doped with As and P are independent of N and, within the experimental errors, γ_S is constant to (27±6) dyn·cm^{-1}. In this framework, the surface wettability of the n-SiO_x samples can be modulated varying both N and the dopant type. Specifically, it doubles at $N \approx 2\cdot10^{15}$ cm^{-3} with respect to the peak baseline value, *viz.* $N \leq 5\cdot10^{14}$ cm^{-3} and $N \geq 4\cdot10^{15}$ cm^{-3}.

The interval of γ_S for the n-SiO_x samples ranges from ≈ 25 to ≈ 50 dyn·cm^{-1}, in agreement to the literature for glass, (52.4 ± 9.9) and (53.9 ± 10.8) dyn·cm^{-1},[26,86] quartz III, (51.4 ± 1.1) dyn·cm^{-1},[87] n-SiO_x, (52.5 ± 1.5) and (52.5 ± 1.5) and (39.64 ± 0.01) dyn·cm^{-1},[88,89] and thermal SiO_2, 45.9 dyn·cm^{-1}.[90] Such values are however lower than the generally accepted values for thick thermal SiO_2 (≈ 80 dyn·cm^{-1})[91] and 3D-silicates like quartz (quartz I in Ref. [87] ≈ 70 dyn·cm^{-1}). This discrepancy between measured and expected γ_S values may indicate some chemical contamination of the n-SiO_x surfaces, which alters the surface properties. A good test bench for surface chemical contaminations is the water contact angle θ_W. In a first approximation, it is representative of the surface wettability, i.e. the cohesion of atoms and molecules to the solid surface: $\theta_W \leq 90°$ corresponds to a surface with a greater wettability (hydrophilic), while $\theta_W \geq 90°$ to a lower one (hydrophobic). The water contact angle θ_W is also linked to γ_S through Equation 1 for which a larger γ_S implies a lower θ_W and *vice versa*. The measured θ_W of the n-SiO_x samples ranges from 52 to 96° where the majority of them are hydrophilic, whereas the remaining samples are hydrophobic. Such θ_W values are however larger than the expected values for clean SiO_2 that should be < 30°.[87,91,92] This is consistent with airborne contaminants deposited on the n-SiO_x surfaces along their storage time in air,[93] and thus the measured θ_W/γ_S is higher/lower than the expected one.

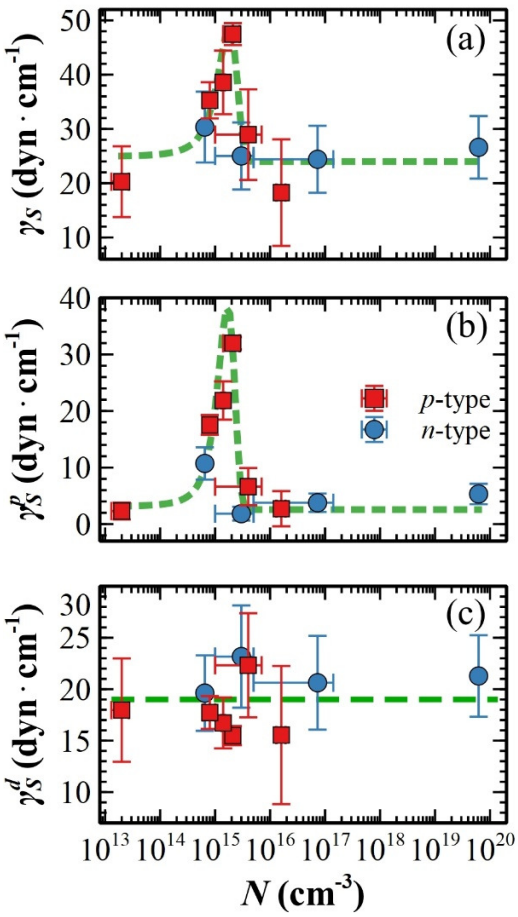

Figure 2. Surface energy γ_S values (a) and correspondent polar, γ_S^p (b), and dispersive, γ_S^d (c), components vs. N. Square red points refer to *p*-type samples, while circular blue points refer to *n*-type samples. Dashed green lines are guide-to-the-eye obtained by fitting data with Gaussian peaks (a, b) and a straight line (c).

As reported previously,[94] the variability of the contact angle θ (for all liquids) on n-SiO_x surfaces depends upon the chemical history of those surfaces. The wafers used in this work were produced by different companies in different periods, therefore their chemical history is unpredictable (cp. to Section 2.1). Advanced or aggressive chemical cleaning methods[95] can be used to clean the n-SiO_x surface and thus obtain the expected contact angles. Besides, the solvent-cleaning process described in Section 2.4 is the most employed process to clean n-SiO_x. Therefore, the experimental results reported in this work are potentially useful for other future research works. Nevertheless, two key points (related themselves) need to be satisfied in view of such limitations: i) the trend of γ_S observed in Figure 2a should be reproducible upon the n-SiO_x regrowth; and ii) airborne contaminants effects should be similar upon the same chemical history (i.e. all n-SiO_x samples have to be exposed to clean room air for the same time period).

The n-SiO_x was removed using HF as described in the RCA Standard Clean procedure,[96] then it was left to regrow for 21 days in clean room air (ISO7 classification, average ambient conditions during regrowth are RH = (80 ± 7) %, $T_A \approx$ 16°C). This time period is long enough to grow the 80% of the n-SiO_x thickness, whereas the saturation thickness can be reached after about one year.[5,66,97]

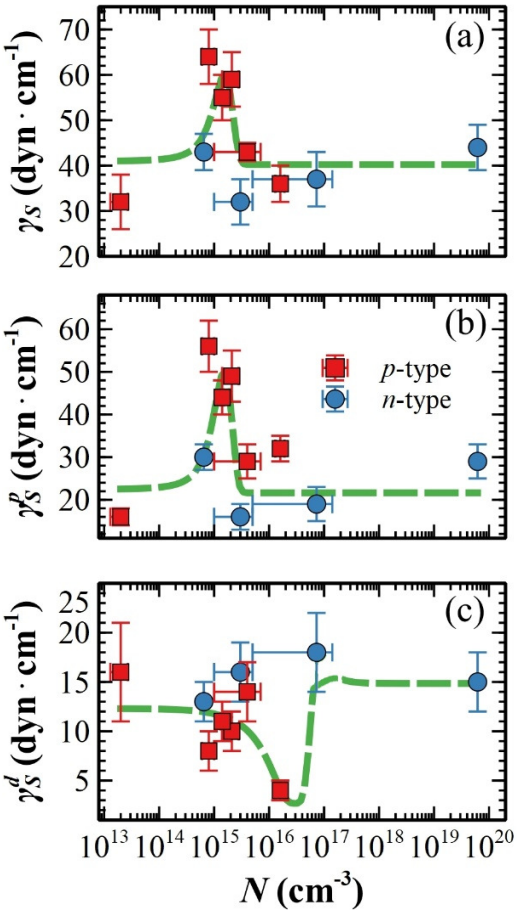

Figure 3. Plots of the surface energy γ_S (a), polar γ_S^p (b) and dispersive γ_S^d (c) components of the n-SiO_x samples regrown for 21 days. Square red points refer to *p*-type samples, while circular blue points refer to *n*-type samples. Dashed green lines are guide-to-the-eye obtained by fitting data with Gaussian (a, b) and Pseudo-Voight (c) peaks.

As shown in Figure 3a, the surface energy γ_S of the regrown n-SiO_x samples preserves its dependence vs. N, with a marked peak in the range [$5\cdot10^{14}$; $4\cdot10^{15}$] cm^{-3}. The maximum of ≈ 65 dyn·cm^{-1} is obtained at $N \approx 2.1\cdot10^{15}$ cm^{-3} (considering the *x*- and *y*-axis absolute errors), while the baseline is shifted to a larger value of (36±8) dyn·cm^{-1}. This result is in agreement with the behavior of RCA-cleaned surfaces reported in the literature:[98] within few hours, the SiO_2 recovers its wettability properties. Comparing one to one the data of "as received" and regrown n-SiO_x samples, the latter curve is shifted up of ≈ 15 dyn·cm^{-1} and its trend is preserved with respect to "as received" samples. The measured θ_W of regrown n-SiO_x samples is reduced ranging from 33 to 73°, thus all samples are hydrophilic.

The polar and dispersive force components, i.e. γ_S^p and γ_S^d, of "as received" n-SiO_x samples are shown in Figure 3b-c. Due to the energy additivity, *viz.* $\gamma_S = \gamma_S^p + \gamma_S^d$, the γ_S plot is the graphical sum of the energy offset due to the dispersive component (Figure 3c) plus the peak shape of the polar component (Figure 3b), that drives the trend observed in the γ_S plot. The dispersive component arises from random

fluctuations in the electron density leading to temporary dipole interactions. As such, the dispersive component does not depend strongly on the atomic structure. The differences in the total surface energies of each n-SiO_x sample is thus mainly due to their polar components, which are ascribable to the dipole moments of the characterization liquids (see Table 2, all liquids are polar) interacting with permanent and/or induced dipoles (e.g. hydrogen bonds) on the n-SiO_x surface by Coulomb interactions. At room temperature, the n-SiO_x surface is partially covered by hydroxyl functional groups (–OH), e.g. ≈ 70%.[70] Such –OH groups are polar and thus responsible for γ_S^p measured by contact angle. Moreover, its trend suggests a dependence of –OH vs. *N*. For regrown n-SiO_x samples, the polar component γ_S^p preserves the trend observed in the "as received" n-SiO_x samples and mainly determines the γ_S peak shape (Figure 3b).

As shown in Figure 2c, the dispersive component is constant, γ_S^d = (19±3) dyn·cm^{-1}, and independent of both *N* and the dopant type. Within the experimental error, this γ_S^d value is equal to the one obtained on bare thermal SiO_2.[91] Since n-SiO_x is amorphous[99], no permanent dipole due to the atomic structure is expected, and thus the peak of the polar component γ_S^p of the *p*-type (and the first value of the *n*-type, see Figure 2b) provides evidence that surface wetting is modulated by the electrostatic force.[100,101] Together with dipoles induced by –OH groups, electrical charges due to *N* or the dopant type (or both) might be responsible for such Coulomb interactions. However, it is not clear if these additional charges are located within the oxide layer or at the Si/SiO_x interface. For regrown n-SiO_x samples, γ_S^d is clearly different with respect to the "as received" n-SiO_x samples (Figure 3c). As expected for the RCA-cleaning SiO_2 surfaces,[102] the initial constant dispersive component, (19±3) dyn·cm^{-1}, is reduced as a whole forming U-shape curve with a baseline of (15±2) dyn·cm^{-1} and a minimum of ≈ 5 dyn·cm^{-1} in correspondence to the γ_S^p maximum (Figure 3c). While the shape is clearly different from the "as received" n-SiO_x samples (Figure 2c), both baselines are equal within the absolute errors, suggesting that γ_S^d depends on time. Actually, the over layer of the n-SiO_x samples takes longer time to stabilize and thus some instabilities are expected.

As crosscheck experiments, γ_S, γ_S^p and γ_S^d of the "as received" n-SiO_x samples were also measured with other three liquids: water, diiodomethane (non-polar) and nitromethane, obtaining the same trends (see Supplementary Materials). Measurements of hysteresis *H* provide other details on surface wettability. The plot of *H* vs. *N* in Figure 4 shows, for the *p*-type samples, a monotonic increase of *H* with increasing *N* for $N < 2{\cdot}10^{15}$ cm^{-3}. For the *n*-type samples, *H* decreases linearly with increasing *N* in a semi-log scale. Regardless of the dopant type, the maximum *H* values are in the range [$7{\cdot}10^{14}$; $2{\cdot}10^{16}$] that includes the range of the peak shape observed in the γ_S plot. The *H* values range from 0.2 to 0.4, in agreement with values reported for Si substrates[45,103] and quartz.[104] As expected for all real surfaces[86] and independently on *N*, *H* is observed for all n-SiO_x samples because of the chemical heterogeneity of their surfaces. Airborne contaminants and/or Si–O–Si groups forms spatial surface domains,[105,106] driving the θ hysteresis. Indeed, if a surface originally has a high surface energy, like oxides,[107] it may adsorb airborne contaminants from the environment to reduce its surface energy. Thus, it becomes more hydrophobic than it originally was.[108]

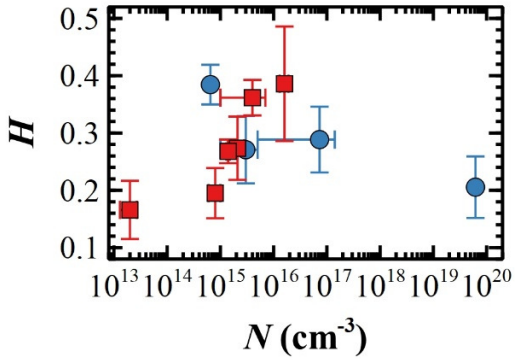

Figure 4. Plot of the hysteresis *H* vs. *N*. Two monotonic trends for the *p*- and *n*-type substrates are clearly visible. Square red points refer to *p*-type samples, while circular blue points refer to *n*-type samples.

3.2 Surface cleanliness of the n-SiO_x samples Highly reproducible surface energy measurements need an evaluation of the surface cleanliness of the n-SiO_x samples. As inferred from the contact angle measurements, the n-SiO_x surface accumulates airborne contaminants forming spatial surface domains or, possibly, a continuous film.[109] Time-of-Flight Secondary Ion Mass Spectrometry (ToF-SIMS) has successfully identified adsorbed organic contaminants such as hydrocarbon, phthalates and aliphatic amines.[110–112] They are originated from the dispersion of volatile organic compounds (VOC) in the cleanroom air. Accordingly, the surface contamination changes with time (almost saturating within few hours),[113] also known as "surface aging", which in turn increases the contact angle θ up to a saturation.[114,115] On silica, which is similar to n-SiO_x, the aging effect causes an increase of the water contact angle of about 10 degree after 20 days of ambient air exposure.[116] This aging effect can be reduced by cleaning the n-SiO_x surface with the solvent-cleaning process prior contact angle measurements (cp. to Section 2.4). As proved in the master thesis of Della Ciana,[36] this procedure grants freshly cleaned surfaces and high reproducible θ measurements.

For a quantitative evaluation, the TD measurements were performed on the sample with the highest expected amount of surface contaminants, i.e. the sample with the highest surface energy γ_S (≈ 47 dyn·cm^{-1}, wafer 5, see Table 1) for which the molecular adsorption from airborne contaminants is the highest.[117] Increasing T_S from 20 (T_A) to 450°C, the contaminants are progressively desorbed, granting a minimal surface contamination.[47] The residual gas due to heating is analyzed with RGA, producing a beam of ions via collisions between the residual gas and the electrons emitted from a hot cathode. The ions are filtered according to their mass-to-charge ratio, *m*/*z*. An output current is measured with a Faraday cup revealing the amount of ions with a given *m*/*z* passing through the filter. These measurements were performed at 20, 100, 200, 300 and 450°C.

As shown in Figure 5, no significant difference can be observed between the n-SiO_x sample and the empty sample

holder (control experiment), even at 450°C, where the contaminants are expected to be fully dispersed in the residual gas. At $T_S \approx 450$ °C, the vacuum pressure rises to $1.5 \cdot 10^{-7}$ mbar and RGA reveals only H_2, CO, CO_2 and H_2O molecules,[12] like the XPS and ToF-SIMS measurements.[111] This result confirms that the storage procedure adopted herein ensures minimal surface contamination.

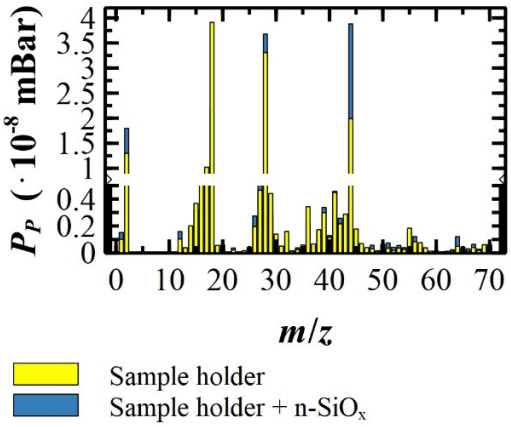

Figure 5. Partial pressures (P_P, in mbar) of the residual gas elements, identified by m/z, for the sample holder (yellow bars) and the sample holder with the n-SiO_x sample (blue bars). The elements are expressed in mbar because their ion currents are singularly proportional to a (partial) pressure[118] whose integral sum returns to the total pressure of the vacuum chamber.

3.3 Surface coverage of the TFOCS SAMs on the n-SiO_x surfaces The airborne contamination of surfaces is relatively fast and unavoidable. On the other hand, it is a necessary step to equilibrate the high reactive –OH groups in air. Prior to functionalization, n-SiO_x samples were cleaned using a stronger cleaning-process (sonication and backing in air, cp. to Section 2.6) than the one based on solvents. This process removes most of contaminations partially restoring the original –OH surface density. Such –OH groups interact with the TFOCS molecules,[119] although the growth mechanisms of SAMs[120] and steric constraints[121] do not allow to form perfectly packed SAMs. Consequently, the surface coverage Θ of SAMs is somehow, but not exactly, proportional to the –OH surface density.

As shown in Figure 6, Θ describes a downward parabola-like in a semi-log scale with a maximum at $N \approx 1.6 \cdot 10^{16}$ cm^{-3} where surface –OH groups is maximized. *Vice versa*, the parabola is upward for Si–O–Si with a minimum at the same N. Accordingly, Θ is clearly dependent on N, but it seems independent of the dopant type.

These parabolic trends agree with what was observed with the γ_S peak in Figure 2, suggesting a key role of the functional groups on γ_S. Moreover, Θ is consistent with the literature where, at room temperature, the n-SiO_x surface is partially coated by –OH groups for about 70 %.[70] As proved by Yu *et al.*,[122] γ_S of glassy silica is increasingly proportional to the surface density of the –OH groups: a higher density means a higher surface energy and thus a more hydrophilic surface (the majority of the "as received" n-SiO_x samples and all regrown ones are hydrophilic). The siloxane bridges Si–O–Si act in the opposite direction, reducing γ_S for an increasing surface density of Si–O–Si.[123,124] Comparing Figures 5 and 1, the maximum (minimum) –OH (Si–O–Si) surface density at $N \approx 1.6 \cdot 10^{16}$ cm^{-3} has $\gamma_S \approx 18$ dyn·cm^{-1}, whereas it increases to ≈ 35 dyn·cm^{-1} for the minimum (maximum) –OH (Si–O–Si) group density at $N \approx 8 \cdot 10^{14}$ cm^{-3}. In view of this result, the Si–O–Si groups influence γ_S more than the –OH ones because the airborne contaminations should reduce the polar contribution of the –OH groups through, for instance, deprotonation.[125] In conclusion, mutual effects of the functional groups modulate γ_S of the n-SiO_x samples reported in Figure 2.

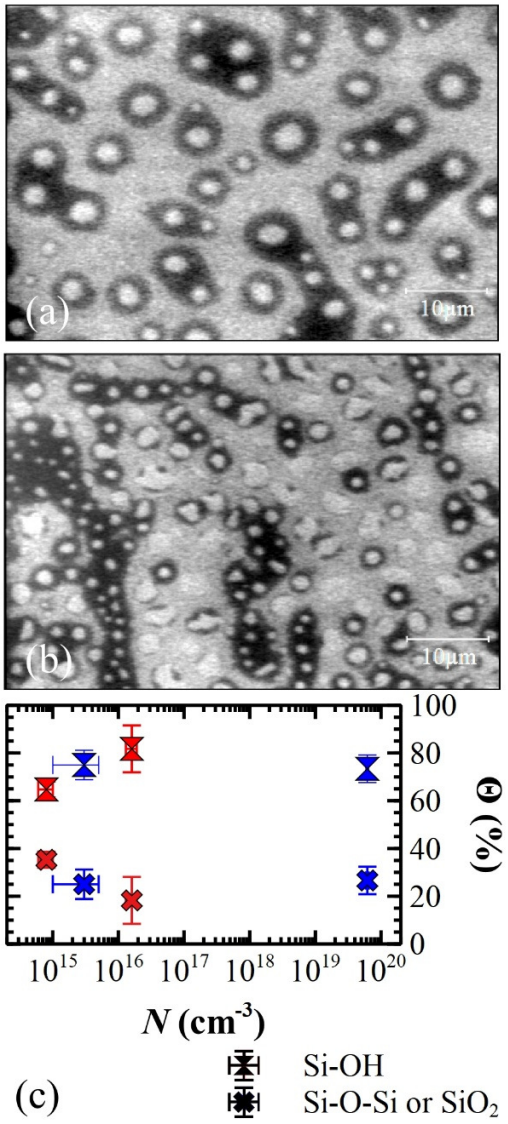

Figure 6. (a, b) SEM images of TFOCS SAMs (bright regions) on the n-SiOx samples (dark regions) with the largest and the lowest Θ (images size 60 × 40 μm²). (c) Plot of Θ (in %) vs. N. for the hydroxyls (tie) and siloxane bridges (cross) for n- (blue) and p-type (red) samples.

3.4 Morphology of the n-SiO_x samples At a first glance, the surfaces of the n-SiO_x samples have similar topographic images, composed of nanometric grains forming a smooth surface with a sub-nanometric roughness (see Figure 7a). Since

topographic images were collected in air, a water layer ≈ 12 Å thick is adsorbed on the n-SiO_x surface due to the RH (≈ 70 %),[72] and it mimics the surface roughness.[76]

The simplest morphological descriptor, shown in Figure 7b, is the rms roughness σ, which is the standard deviation $\sigma = \langle(h-\langle h\rangle)^2\rangle$ of the distribution of the film height h and the standard deviation error is its absolute error.[59] If $\Delta\sigma$ is smaller than the z sensitivity of the AFM piezoelectric tube, i.e. 0.025 nm,[126] the error bar is set to the z sensitivity (or a multiple of it), while the σ values are approximated to the closest multiple value.

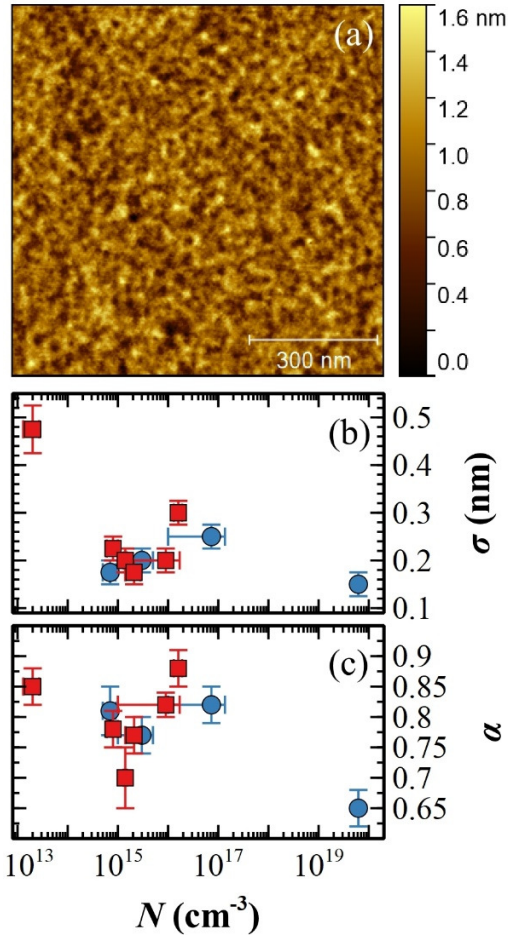

Figure 7. (a) AFM topographic image of a n-SiO_x surface. Roughness σ (b) and roughness exponent α (c) plots vs. N. Square red points refer to p-type samples, while circular blue points refer to n-type samples.

The roughness plot of Figure 7b shows a marked difference between p- and n-type doping, as for the surface energy γ_S. The p-type samples describe an upward parabola-like trend in a semi-log scale, specular to the downward parabola-like of the surface energy γ_S. This trend suggests a correlation between σ and γ_S for which a smoother surface corresponds to a larger surface energy: the minimum σ coincides with the maximum γ_S at $N \approx 2.1\cdot10^{15}$ cm^{-3}. The n-type samples follow a similar trend but inverted and less prominent.

The n-SiO_x samples present self-affine surfaces that can be studied using the Height-Height Correlation Function (HHCF).[60,127] The HHCF in a log-log plot shows two different regions, correlated and uncorrelated, characterized by a slope and a *plateau*, respectively (see Supplementary Materials). Such regions are separated at ζ, also defined correlation length, at which HHCF forms a "knee".[58] For all the n-SiO_x surfaces, $\zeta \approx 20$ nm corresponds to the average grain size of the oxide films.[128] In the correlated region, HHCF is $\propto L^{2\alpha}$ where L is the length between any two points of the surface and α is the roughness exponent.[129] A surface profile with α that tends to 0 corresponds to a smooth surface, while $\alpha \to 1$ is representative of a jagged one.[130] As shown in Figure 7c, α for the n-SiO_x samples is always larger than 0.65, so the surface profiles are jagged and dependent on the dopant. Like roughness, α for the p-type samples describes an upward parabola-like in a semi-log scale with a minimum at $N \approx 2.1\cdot10^{15}$ cm^{-3} and two maxima at $\approx 2\cdot10^{13}$ and $\approx 1.6\cdot10^{16}$ cm^{-3}. On the other hand, α is equal to ≈ 0.8 for the n-type samples then it decreases to ≈ 0.65 for the largest N, *viz.* $\approx 6.2\cdot10^{19}$ cm^{-3}. A comparison between the topographic profiles for minimum and maximum α of the p-type samples can provide some insights on the surface wettability.[131]

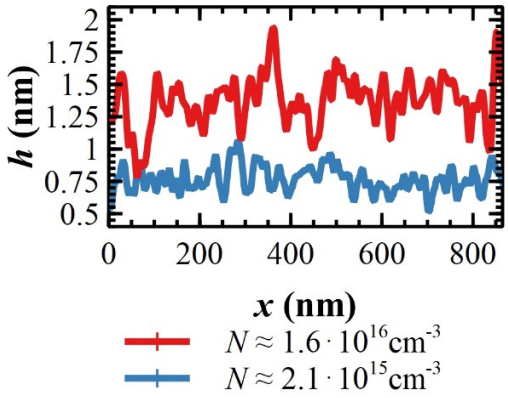

Figure 8. Topographic profiles of a n-SiO_x surface (a). Roughness σ (b) and Hurst exponent H_h plots vs. N.

Figure 8 suggests the physical reason of the α modulation: a profile with relatively larger and smoother oscillations (red profile) has a relatively larger α value, while relatively small oscillations forming a more jagged profile (blue profile) has relatively lower α value.[132] The roughness exponent α, equivalent to the Hurst exponent, is related to the fractal dimension D_f of a surface through the simple relationship $D_f = 3 - \alpha$, where, in agreement to the aforementioned observations on the topographic profiles, a larger value of α corresponds to a locally smooth surface, while a smaller one corresponds to more locally jagged morphology.[129,133] The α vs. N plot in Figure 7c is therefore inverted in the D_f vs. N plot. As proposed by Packham,[134] the surface energy γ_S is proportional to $\zeta^{2-Df} = \zeta^{\alpha-1}$, so the smaller is α the smaller is γ_S, being ζ constant for all the n-SiO_x samples. This agrees with the evidence that the larger is the roughness, the higher is the surface energy.[134] The surface roughness is therefore not responsible for the large modulation of γ_S observed in Figure 2.[135]

The scale-length of σ is indicative of a surface morphologically clean. In fact, the "as received" n-SiO_x samples exposed to airborne contaminations present several molecular aggregates (tens of nm height and hundreds of nm wide) on

their surfaces.[136] As proved by the topographic image of Figure 7a (and others topographic images reported in the Supplementary Materials), such possible aggregates are removed by using a solvent-cleaning process, leaving the n-SiO_x surface featureless. Water contact angle measurements have shown that the n-SiO_x surfaces are not chemically clean and, as modelled in Ref. [39], airborne contaminants were possibly adsorbed flat on the n-SiO_x surface in order to equilibrate –OH groups. Topographic AFM images of Figure 7a and in the Supplementary Material seem confirm this model since no molecular aggregates are visible (or, at most, they are thinner than the AFM *z*-sensitivity, i.e. 0.025 nm).[76] On the contrary, such molecules can be indirectly detectable by measuring the Skewness and Kurtosis of surfaces height distributions.[137–139] Both statistical parameters show a minimum at $N \approx 2.1 \cdot 10^{15}$ cm^{-3}, consistent with less adsorbed airborne contaminants that are, possibly, more conformal to the surface roughness with respect to others n-SiO_x samples (see Supplementary Materials).

3.5 Ellipsometric measurements of the n-SiO_x As reported in the literature,[7,97,140,141] the n-SiO_x thickness t calculated from ellipsometric data is always below 5 nm for all N values. In such a thickness range, the ellipsometric parameter Δ carries the most of the information on t and the n-SiO_x refractive index n, whereas the other parameter Ψ is largely insensitive on both.[71] As largely recognized in the literature,[61,142] the simultaneous determination of t and n of ultrathin films from solely Δ data is not practically feasible, except for special experimental arrangements capable of decoupling the t and n effects from both Δ and Ψ parameters. The inverse problem, i.e. evaluation of t from Δ if n is fixed, is instead an easy task to achive.[11,97] Optical data are therefore fixed for the layers shown in the n-SiO_x model (see Figure 1), except for the thickness of the n-SiO_x (bulk) layer, t', that is calculated by fitting ellispometric data. This choice avoids speculations on the spectral form of the dielectric constants of the layers.

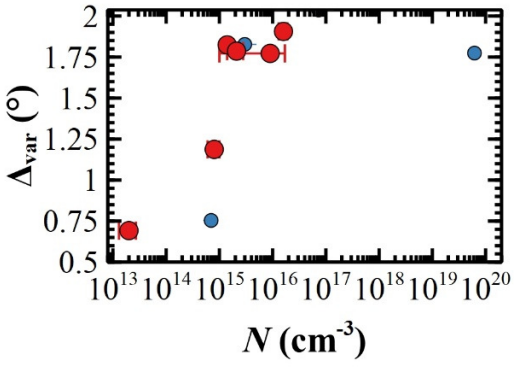

Figure 9. Plot of the Δ_{var} vs. N obtained by using the ellipsometric parameter Δ as shown in Equation 6. Circular red points refer to *p*-type samples, while the blue ones refer to *n*-type samples.

In the framework of the model air/oxide/substrate,[93] layers composing the oxide (the water layer included, see Figure 1) have refractive indexes smaller than the one of Si (n = 3.8823 at 633 nm). The value of Δ measured at 633 nm is therefore smaller than the bare Si substrate Δ_{Si} (Δ_{Si} = 179.80, see for instance Ref. [78]), becoming even smaller if the thickness t increases or n decreases. Accordingly, the experimental shift (variation) of Δ, Δ_{var}, can be measured as:

$$\Delta_{var} = \Delta_{Si} - \Delta \qquad (6)$$

The trend of Δ_{var} at 633 nm is strongly dependent on N: it is relatively low for $N < 10^{15}$ cm^{-3}, then it increases within a transition region 10^{15} cm^{-3} < $N \leq 4 \cdot 10^{15}$ cm^{-3}, after which it saturates for $N > 4 \cdot 10^{15}$ cm^{-3} (see Figure 9). This result suggests a variable oxide thickness on N, thinner for the lower N and thicker for the higher ones. Being Δ_{var} derived from experimental data, the trend observed in Figure 9 is independent to the model adopted in the simulation.

Table 4. n-SiO_x thicknesses as calculated from SE data[d]

N (cm^{-3})	-type	σ (nm)	t' (nm)	t (nm)
$(2.0 \pm 0.7) \cdot 10^{13}$	p	0.5 (0.45)	0.1 (0.44)	1.1 (0.89)
$(7 \pm 2) \cdot 10^{14}$	n	0.2	0.54	0.94
$(8 \pm 2) \cdot 10^{14}$	p	0.2	0.84	1.24
$(1.4 \pm 0.1) \cdot 10^{15}$	p	0.2	1.39	1.79
$(2.1 \pm 0.7) \cdot 10^{15}$	p	0.2	1.37	1.77
$(3 \pm 2) \cdot 10^{15}$	n	0.2	1.40	1.80
$(9 \pm 8) \cdot 10^{15}$	p	0.2	1.34	1.74
$(1.6 \pm 0.3) \cdot 10^{16}$	p	0.2	1.48	1.88
$(7.3 \pm 6.8) \cdot 10^{16}$	n	0.2	1.60	2.00
$(6.2 \pm 0.3) \cdot 10^{19}$	n	0.15	1.39	1.69

[d] n-SiO_x thicknesses, t, calculated as $t' + 2 \cdot \sigma$ where t' is the thickness of the n-SiO_x (bulk) layer as evaluated by fitting SE data, and σ is the roughness measured by AFM (cp. to Figure 7b). Since fitting has an expected margin of error of about the 10 %, σ is rounded to ≈ 0.2 nm for all N except for the N interval limits, i.e. ≈ 0.5 nm for $N \approx 2.0 \cdot 10^{13}$ cm^{-3} and ≈ 0.15 nm for $N \approx 6.2 \cdot 10^{19}$ cm^{-3}. For $N = (2.0 \pm 0.7) \cdot 10^{13}$ cm^{-3}, the simulation was repeated by using a different composition of the n-SiO_x (bulk) layer (see Table 3) and leaving free the thickness of the n-SiO_x (surface) layer. The calculated thickness in such conditions is $t \approx 0.89$ nm (values in brackets) that is consistent with $t \approx 1.1$ nm, as calculated with the method adopted for all N.

To obtain quantitative results from experimental Δ-Ψ spectra, the oxide layer was modelled as described in Section 2.8. The total thickness t of the n-SiO_x is strictly correlated to the model assumptions; if the water layer and the roughness are neglected, $t = t'$ and the n-SiO_x thickness will be underestimated. Conversely, the oxide model is closer to a "real" n-SiO_x sample if they are considered. As explained in Section 2.8, the water layer thickness was fixed to ≈ 0.4 nm whereas the roughness is determined by AFM measurements (cp. Section 3.4 and Table 4). Although composed of two half-spaces, the n-SiO_x (bulk) layer is considered as a whole with thickness t'.

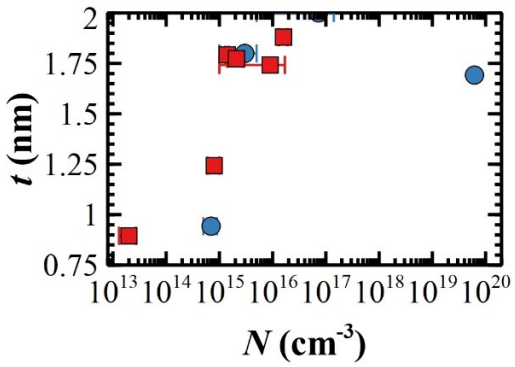

Figure 10. Thickness $t = t' + 2\cdot\sigma$ of n-SiO_x vs. N as obtained from ellipsometric measurements. Square red points refer to *p*-type samples, while circular blue points refer to *n*-type samples.

As expected, the n-SiO_x thickness t follows Δ_{var} data (Figure 10), hence t is thinner for $N < 10^{15}$ cm^{-3}, then it increases within a transition region 10^{15} cm^{-3} < $N \leq 4\cdot10^{15}$ cm^{-3}, after which it saturates to thicker value for $N > 4\cdot10^{15}$ cm^{-3}. Moreover, t trend is qualitatively similar to a step-like function, *viz*. a logistic one, whit a step foot at (0.9 ± 0.1) nm, the thinnest t, and a step head at (1.81 ± 0.04) nm, the thickness saturation (see Supplementary Materials).

These results confirm the validity of the model adopted to describe the n-SiO_x. The surface roughness and the water layer have a moderate impact on the calculated thickness t'. The method of minimum χ^2 estimation returns values < 1, indicating good agreement between the experimental data and simulated model and discrepancies smaller than the expected 10 %.

The n-SiO_x sample with the lowest N, i.e. ≈ $2\cdot10^{13}$ cm^{-3}, turn out to be more complex. The sample roughness σ is the highest, i.e. ≈ 0.5 nm (cp. Figure 7b), but the thickness t is expected to be the thinnest, i.e. lower than 1 nm. Since $2\cdot\sigma$ is the average peak-to-valley distance that characterizes roughness oscillations, the morphology of this sample should be dominated by the roughness. On this basis, data simulation for this specific sample was done in two ways: first, t is calculated by using constraints of other samples and, second, a specific composition of a "rough layer" (Si – 25 %, SiO_2 – 25 %, Voids – 50 %, see Table 3) was introduced and the simulation constraint of fixed roughness was removed. Both simulations return consistent t values of 1.1 and 0.89 nm for the first and the second model, respectively (see Table 4, in average ≈ 1 nm). The discrepancy between them is within the expected error (± 10 %) and χ^2 estimation has values < 1 in both cases.

The n-SiO_x thickness changes suddenly at $N \approx 10^{15}$ cm^{-3}, within the interval [$5\cdot10^{14}$; $4\cdot10^{15}$] cm^{-3} where the surface energy γ_S presents its maximum. Moreover, t seems independent of the doping type having a minimum and a maximum thickness for both doping types. Notably, the maximum thickness is consistent with the self-limited growth theory of n-SiO_x.[143,144] As reported in the literature,[145] airborne contaminants might influence the accuracy of t measurements thus increasing its absolute error.

3.6 Chemical composition of the n-SiO_x layers As obtained from the XPS measurements, the chemical elements composing the n-SiO_x samples are: C (C 1s, 284.6 eV), O (O 1s, 532.2 eV) and Si (Si 2p, 99.0 eV – see Table 5 and Supplementary Materials). Their chemical states agree with the ones found by Morita *et al.*[97] for Si substrates covered with a n-SiO_x layer. Plotting data of Table 5 (see Supplementary Materials), the Si 2p percentage decreases slightly linearly with increasing N, while C 1s signal increases. Consequently, the oxygen atoms O 1s are roughly constant. The C 1s peak identifies a carbonaceous contamination (mostly hydrocarbons)[146] adsorbed on the n-SiO_x surface and produced by VOC dispersed in air.[100,111,147] In agreement with the model for adsorption of organic contaminants on a n-SiO_x surface in a cleanroom,[148,149] the contamination layer was measured as ≈ 0.16 nm thick,[57] herein rounded to ≈ 0.2 nm to consider the C 1s variations of the n-SiO_x samples. This approximation seems reasonable in view of the minimum roughness measured with AFM (≈ 0.2 nm, see Figure 7b). If the thickness of the contamination layer was larger, a smoothening effect in the topographic profiles (Figure 8) should be expected[150] and the large roughness variation observed in Figure 7b should flatten out.

Table 5. Chemical elements of n-SiO_x[e]

N (cm^{-3})	Si 2p (at.%)	O 1s (at.%)	C 1s (at.%)
$(2.0\pm0.7)\cdot10^{13}$	61.3 ± 1.0	27.4 ±1.0	10.3 ± 1.0
$(8\pm2)\cdot10^{14}$	61.3 ± 1.0	28.1 ±1.0	10.6 ± 1.0
$(2.1\pm0.7)\cdot10^{15}$	64.4 ± 1.0	26.9 ±1.0	8.7 ± 1.0
$(1.6\pm0.3)\cdot10^{16}$	50.2 ± 1.0	26.8 ±1.0	23.0 ± 1.0
$(7.3\pm6.8)\cdot10^{16}$	59.0 ± 1.0	29.8 ±1.0	11.2 ± 1.0
$(6.2\pm0.3)\cdot10^{19}$	53.2 ± 1.0	28.8 ±1.0	18.0 ± 1.0

[e] Chemical elements in atomic percentage (at.%), i.e. the percentage of one kind of atom relative to the total number of atoms, composing the samples.

Most of the O atoms are bond to the Si ones, forming a variety of Si oxides, which are spatially distributed within the entire thickness of the amorphous n-SiO_x layer. Specifically: i) an interfacial layer near the Si substrate (Si) that consists of few atomic layers containing Si atoms in intermediate oxidation states, i.e., Si^{1+} (Si_20), Si^{2+} (SiO), and Si^{3+} (Si_20_3). This interfacial region occupies ≈ 50 % of the whole n-SiO_x thickness.[65] Compared to an ultrathin thermal SiO_2 with a similar thickness (≈ 2 nm), it occupies ≈ 20 %, i.e. few SiO_2 monolayers;[151,152] ii) the remaining ≈ 50 % of the n-SiO_x thickness is occupied by an over layer composed solely of Si^{4+} (SiO_2).[65–68] The Si intermediate-oxidation states can be discriminated with the Si 2p core-level chemical shifts.[153] Performing high resolution XPS measurements of the Si 2p signal, the Si intermediate-oxidation states can be discriminated using as references the binding energies (BE) of both the Si substrate and the Si^{4+} (SiO_2), which are 99 and 103 eV, respectively. The measured shifts of the core-level binding-energies with respect to the Si substrate are: 1.75, 3.0, and 3.9 eV for Si^{2+}, Si^{3+} and Si^{4+}, respectively. These shifts are in agreement with the ones obtained by Himpsel *et al.*.[153] The shift of the Si^{+1} energy is not measurable being it lower than the instrumental sensitivity (XPS measurements were performed with a laboratory scale system). The Si intermediate-oxidation states are obtained from the fit of the XPS Si 2p signal with pseudo-Voigt functions, referring them to the Si 2p doublet with a fixed energy separation, *viz*. Si $2p_{1/2}$ –Si

$2p_{3/2}$ = 0.63 eV, an identical (constrained) FWHM for Si $2p_{1/2}$ and Si $2p_{3/2}$ and a constrained area ratio (1:2) between Si $2p_{1/2}$ and Si $2p_{3/2}$ (see Supplementary Materials). This procedure is repeated for all the n-SiO_x samples with increasing N.

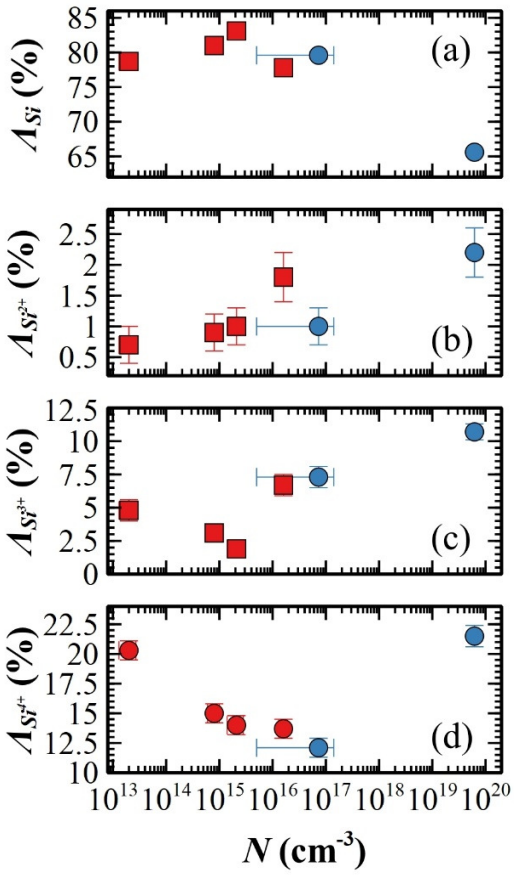

Figure 11. Peak areas Λ_i vs. N of the Si substrate (a) and intermediate-oxidation states Si^{2+} (b), Si^{3+} (c) and Si^{4+} (d). Square red points refer to *p*-type samples, while circular blue points refer to *n*-type samples.

As a first result, the XPS measurements confirm that the samples consist of a Si substrate covered with a n-SiO_x layer; actually, increasing the angle between the surface normal and the analyzer (grazing incidence), the signal from the n-SiO_x increases (not shown).

The Si substrate and its intermediate-oxidation states (Si, Si^{2+}, Si^{3+}, Si^{4+}) vs. N are shown in Figure 11. To compare them, the entire area of the XPS spectra of the Si 2p signal (Λ, in percentage, is 100 %) is used as reference as previously done by Himpsel *et al.*[153] The deconvolution of the Si 2p spectra in peaks centered at a specific BE permits to measure the peak area Λ_i of each component, i.e. Λ_i is the area of the i peak referred to Si, Si^{2+}, Si^{3+} or Si^{4+}. As it can be seen in Figure 11, the chemical composition of the n-SiO_x layer depends markedly on N. The Si substrate peak, Λ_{Si}, increases slightly up to $N \approx 2.1 \cdot 10^{15}$ cm^{-3} and then it decreases rapidly with increasing N (Figure 11a). The n-SiO_x thickness, t, which increases from less than 1 nm to about 2 nm in the same N range, is responsible for the partial screening of the Si substrate signal. At the opposite side, the SiO_2 describes a parabolic-like trend in a semi-log scale with a minimum just above $N \approx 1 \cdot 10^{16}$ cm^{-3} where Λ_{Si4+} is reduced by half (Figure 11d). Inspecting the Λ_i percentages, the XPS signals are mainly originated from the Si substrate and the SiO_2 over layer. Other intermediate-oxidation states, Si^{2+} and Si^{3+}, evolve with N forming a variable transition region between Si and SiO_2: Λ_{Si2+} increases roughly linearly with N while Λ_{Si3+} has a cusp-like trend with a minimum at $N \approx 2.1 \cdot 10^{15}$ cm^{-3} (Figure 11b and 11c). The XPS measurements do not depend on the dopant type.

A simple model proposed by Oh,[152] based on XPS data and numerical simulations, limits such a transition region to three atomic layers composed of Si and O atoms (4.1 Å thick), where the intermediate-oxidation states are sequential: Si^{1+}/Si^{2+} are in contact with the Si substrate, Si^{2+}/Si^{3+} are in the middle of the interfacial region, and lastly Si^{3+}/Si^{4+} are just below the SiO_2. This simplified model was refined by Bongiorno *et al.*[154] performing numerical simulations on XPS data available in the literature. From these simulations, the transition region presents fixed atomic ratios between the intermediate-oxidation states, i.e. Si^{1+}:Si^{2+}:Si^{3+} = 1:2:3, and its thickness is larger than three atomic layers, increasing up to 10 Å due to disordered and distorted atomic bonds.[155]

The role of the doping concentration N on the transition region has been studied for moderate ($N \approx 6 \cdot 10^{15}$ cm^{-3}) and heavy ($N \approx 10^{20}$ cm^{-3}) doped Si substrates with P and B dopants, observing a significantly higher amount of Si^{3+} in heavily P doped Si substrates.[5,6,156] The description of the transition region emerging from these studies is more complex than a sequence of intermediate-oxidation states along its thickness, comprising overlapping zones and dependence on N (as seen in Figure 11).[5,6] The XPS spectra collected before and after the TD experiments corroborate this model (cp. Section 3.2). As expected, the chemical composition of the oxide is preserved because $T_S \approx 450$ °C is significantly lower than 700 – 800 °C, needed to decompose it.[157] However, a little appreciable variation can be found in the Si 2p fit (spectra not reported): i) before TD, Λ_{Si3+} and Λ_{Si4+} are 3.7 and 14.5 %, respectively; ii) after TD, they shift to 2.1 and 15.7 %. As reported in the literature,[97] this is possibly due to an initial de-oxidation of Si-O or Si-OH groups. Lastly, the C 1s peak does not change, i.e. carbonaceous contaminations are preserved at each T_S and they can only be removed chemically.

Following the original idea of Morita,[97] the XPS data are also useful to evaluate the n-SiO_x thickness t. Seah *et al.* proposed a simple method to measure ultra-thin t using the equation:[151]

$$t = \ell_{SiO_2} \cdot \cos\varepsilon \cdot ln\left(1 + \frac{\Lambda_{Si^{4+}} + 0.75 \cdot \Lambda_{Si^{3+}} + 0.5 \cdot \Lambda_{Si^{2+}} + 0.25 \cdot \Lambda_{Si^{1+}}}{R_0 \cdot (\Lambda_{Si} + 0.75 \cdot \Lambda_{Si^{1+}} + 0.5 \cdot \Lambda_{Si^{2+}} + 0.25 \cdot \Lambda_{Si^{3+}})}\right) \quad (7)$$

where ℓ_{SiO2} is the inelastic mean free path (29.64 Å for Mg Kα), ε is the emission angle of the detected electrons with respect to the surface normal; herein ε = 0 degree, and R_0 = 0.9329 is an experimental scaling factor.[158]

Compared to t measured with ellipsometry, the one measured with XPS produces smaller values (cp. Figure 10 and Figure 12); probably, the spatial distribution of the atoms composing the intermediate-oxidation state (Si^{3+}, Si^{2+} and Si^{1+}) confined at the Si/thermal SiO_2 interface is oversimplified in the formulation of Equation 7, devised for ultrathin thermal SiO_2. As shown in Figure 12, this oversimplification produces smaller values with a mild correlation with N, leaving t constant to ≈ 0.55 nm up to ≈ $1 \cdot 10^{17}$ cm^{-3}, after which it increases to ≈ 1 nm. As for the ellipsometric measurements, t is not apparently influenced by the dopant type.

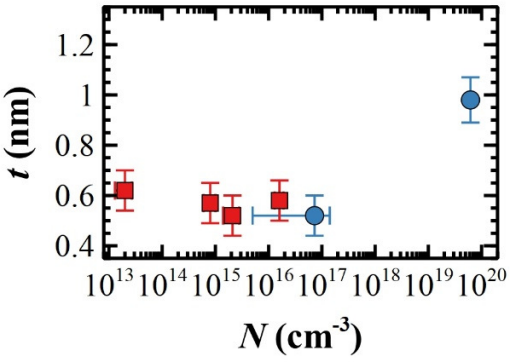

Figure 12. Thickness t of the n-SiO_x layer vs. N, obtained with XPS. Square red points refer to *p*-type samples, while circular blue points refer to *n*-type samples.

3.7 Oxide and interfacial charges measured by Kelvin Probe In Kelvin Probe (KP) measurements, a contact potential difference (CPD, in V) is generated between the surfaces of a metal, the KP tip, and a semiconductor covered with an ultra-thin oxide layer, the n-SiO_x sample, brought both nearby (separated by 0.2 mm) and in electrical contact. Their Fermi levels equalize and electrons in the material with the lower WF flow to the one with the higher one. The KP tip, an Au disk with diameter of 2 mm, and the n-SiO_x sample form a parallel plate capacitor, on which equal and opposite surface charges are accumulated. The voltage developed over this capacitor, *viz.* CPD, is measured applying an external backing potential to the capacitor until the surface charges disappear. The WF is usually defined as an energy measured in eV, whereas the potential CPD obtained from the KP measurements is measured in V. For consistency, the energy is converted in potential through the relationship WF (in V) = WF (in eV)/e, where e is the elemental charge. If the work function of the tip, WF_T, can be obtained from calibrating it on a reference sample (cp. Section 2.10), the work function of the sample, WF, is related to the CPD as:[159]

$$\mathrm{WF} = \mathrm{WF_T} - \mathrm{CPD} \qquad (8)$$

Equation 8 is valid for ideal and flat band conditions.[160] By definition, the WF (in eV) of a bare semiconductor, i.e. without the n-SiO_x, is:

$$\mathrm{WF} = E_C - E_F + E_{EA} \qquad (9)$$

where E_C is the conduction band energy, E_F the Fermi energy and E_{EA} the electronic affinity (for Si, E_{EA} = 4.05 eV). Equation 9 in potentials is:

$$\mathrm{WF} = V_C - V_F + \chi \qquad (10)$$

where χ = 4.05 V. Being χ independent of the doping,[161] the WF changes are due to the modulations of Fermi energy induced by N. In this work N is adopted for both dopant types, while N_A and N_D are usually used in semiconductor physics for distinguishing *p*-type and *n*-type semiconductors, respectively. Accordingly, readers have to consider N as N_A or N_D for *p*- or *n*-type n-SiO_x samples, respectively.

The position of the Fermi level V_F for extrinsic and non-degenerate semiconductor (i.e. with moderate doping concentration), can be written as:[162]

$$(a) \quad V_C - V_F = kTln\left(\frac{N_C}{N}\right) \qquad (b) \quad V_F - V_V = kTln\left(\frac{N_V}{N}\right) \qquad (11)$$

where V_V is the potential relative to the valence band energy E_V ($V_V = E_V/e$), while N_C and N_V are the effective density of states (in cm^{-3}) in conduction and valence band, respectively.

Combining Equations 12 and 11:

$$(a) \quad \mathrm{WF} = \chi + kTln\left(\frac{N_C}{N}\right) \qquad (b) \quad \mathrm{WF} = V_B + \chi - kTln\left(\frac{N_V}{N}\right) \qquad (12)$$

where V_B is the potential relative to the bandgap E_B and $V_B = V_C - V_V$. As shown in Equations 13, WF vs. N describes a straight line in a semi-log plot for both *n*- (a) and *p*-type (b) semiconductors. Using logarithm properties, $ln(N_{C,V} \cdot N^{-1}) = ln(N_{C,V}) - ln(N)$, the straight line has negative and positive slopes for *n*- (Equations 13a) and *p*-type (Equations 13b) semiconductors, respectively.

The WF data of the n-SiO_x samples shown in Figure 13 do not follow the straight lines predicted by Equation 12, which are therefore valid only for bulk Si. Such discrepancies are due to the n-SiO_x covering the Si surface. Charges within and on the surface of this passivation layer cause the Fermi level pinning, i.e. band bending of the energy levels (including the vacuum level) of a surface potential Φ_0 (in V),[163] so CPD' ≠ WF_T – WF (CPD' is the measured potential, not the ideal CPD for a bulk Si). The potential Φ_0 is zero in flat band condition (CPD' = CPD),[164] positive for depletion and inversion, and negative for accumulation. According to the Bardeen model,[165] Φ_0 specifies the level below which all the surface states must be filled for charge neutrality at the Si surface, and roughly it is ≈ ⅓·V_B. The n-SiO_x on the Si surface contains, as summed up by Sze,[164] fixed, trapped and interfacial charges and mobile ionic charges together with an additional electric dipole in the transition region.[166,167] It is reasonable therefore to suppose that a depletion or an accumulation layer is formed for both *n*- and *p*-type samples across the n-SiO_x/Si interface due to a mutual charge arrangement. As explained by Schroder,[168] such depletion (or accumulation) layer is due to image charges in Si induced by the electrical charges on the n-SiO_x surface. Depending on the sign of surface charges, the majority carriers in Si flow towards (accumulation) or outwards (depletion) the n-SiO_x/Si interface.

Using Equation 10 and Figure 1 of Ref. [165] (referred to a *n*-type Si), the work function at the interface of the sole Si affected by band bending, WF', is:

$$WF' = |V_B - \Phi_0| + \chi \approx \frac{2}{3}V_B + \chi \qquad (13)$$

The surface states density (≈ 10^{12} cm^{-2} in Si)[169] is usually larger than the intrinsic Si surface charge density (≈ 10^6 cm^{-2}), therefore Φ_0 is independent of N,[170] as well as E_B that is independent of N for $N < 10^{17}$ cm^{-3}. Samples 1 and 2 in Table 1 are affected by a slight E_B reduction, but this effect is neglected in the context of this manuscript.[171] In the end, Equation 13 is independent of N.

The dependence of WF' on N is recovered from the oxide charge density ρ_{ox} ($C \cdot cm^{-3}$) and the surface charge density Q_S ($C \cdot cm^{-2}$) on the oxide surface (as shown in Figure 5b of Ref. [168]). It is not possible to know the exact distribution ρ_{ox} of charges in the n-SiO_x so, for convenience, it is represented as an effective sheet of charges with surface density Q ($C \cdot cm^{-2}$) placed at distance x_C from the n-SiO_x/Si interface, i.e. $\rho_{ox} = Q \cdot \delta(x - x_C)$ where $\delta(x - x_C)$ is a Dirac delta function.[172] On the other hand, the net charge Q_S of the n-SiO_x surface, either positive or negative, is generated by: i) the type of –OH groups, i.e. isolated, germinal, vicinal or H-bonded;[173] ii) the bond angles of the Si–O–Si groups;[174] and iii) the surface defects produced by stress and strain of the oxide when the –OH groups interact with VOC for equilibrating the n-SiO_x surface.[175] Such net charge Q_S generate image charges in the Si,[168] and so it is correlated to N, whereas there is no evidence that ρ_{ox} depends on N.[164]

As observed by ac Surface PhotoVoltage,[176] Q_S induces a surface potential V_S that is detectable only in the depletion/inversion region, *viz.* if Q_S is positive for p-type Si or negative for n-type Si.

For a small perturbation of the thermodynamic equilibrium, V_S produced by the depletion region of width w at the n-SiO_x/Si interface is:[177]

$$V_S = \frac{eNw^2}{2\varepsilon_{Si}} \qquad (14)$$

where $\varepsilon_{Si} = \varepsilon_0 \cdot \varepsilon_r$ ($F \cdot cm^{-1}$) is the vacuum permittivity ε_0 times the relative permittivity of Si (11.68). On the contrary, $V_S = 0$ in charge accumulation.

To measure the effect of work function differences and charge density on CPD, the flat-band condition V_{FB} of MOS capacitor can be employed.[160] In the depletion condition, CPD' due to WF' is:[168]

$$CPD' = V_{FB} + V_{air} + V_{ox} + V_S \qquad (15)$$

Since under good experimental conditions there is no charge density in the air, Equation 15 reduces to:

$$CPD' = V_{FB} + V_{ox} + V_S \qquad (16)$$

In accumulation, Equation 16 is independent of N since $V_S = 0$ but this in contradiction with the data reported in Figure 13. On the other hand, this observation suggests that the n-SiO_x samples are always in the depletion condition for both n- and p-type, in agreement with ac Surface PhotoVoltage results.[176]

Integrating the charge density ρ_{ox} described by a delta Dirac function at x_C, the n-SiO_x potential drop V_{ox} is then given by:[172]

$$V_{ox} = \frac{e \cdot x_C \cdot Q}{\varepsilon_{ox}} = \frac{e \cdot t \cdot \left(\frac{x_C}{t}\right) \cdot Q}{\varepsilon_{ox}} \qquad (17)$$

where $\varepsilon_{ox} = \varepsilon_0 \cdot \varepsilon_r$ ($F \cdot cm^{-1}$) is the vacuum permittivity ε_0 times the relative permittivity of n-SiO_x (3.9, assumed equal to the thermal one).

The flat-band voltage V_{FB}, i.e. CPD of Equation 8, is:[160]

$$V_{FB} = CPD \approx CPD' - \frac{e \cdot t \cdot \left(\frac{x_C}{t}\right) \cdot Q}{\varepsilon_{ox}} - \frac{eNw^2}{2\varepsilon_{Si}} \qquad (18)$$

which is

$$WF' \approx WF - \frac{e \cdot t \cdot \left(\frac{x_C}{t}\right) \cdot Q}{\varepsilon_{ox}} - \frac{eNw^2}{2\varepsilon_{Si}} \qquad (19)$$

Equation 19 correlates the measured WF' to the WF in a flat band condition (Equation 8). The bulk WF of Si crystal (100) n- and p-type doped is 4.85 V, which is larger than WF' data (see Figure 13), thus giving indirectly evidence of a potential due to the oxide and the depletion layer (see Equation 19).

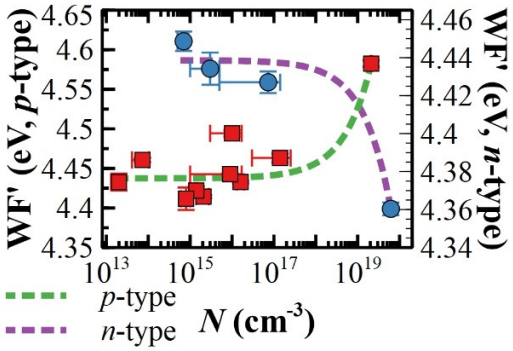

Figure 13. Plots of WF vs. N for p- (left y-axis) and n-type (right y-axis). Square red points refer to p-type samples, while circular blue points refer to n-type samples.

Equation 19 has been used to fit the experimental WF' values using as fitting parameters the oxide charge density Q times the ratio $x_C \cdot t^{-1}$, the depletion layer width w and the charge sign, i.e. sgn(eQ) and sgn(eNw) that is negative or positive for electrons or holes, respectively. The oxide thickness t measured with ellipsometry is function of N, increasing monotonically vs. N and independent of the dopant type (Figure 9). Nevertheless, its dependence on N is a step-like function with an abrupt thickness change at $N \approx 10^{15}$ cm^{-3}. For simplicity without losing generality, t has two values: $t_1 \approx 0.97$ nm and $t_2 \approx 1.81$ nm (see Supplementary Materials). Equation 19 must be satisfied for both the thickness values, so the fitting parameter $(x_C \cdot t^{-1}) \cdot Q$ must be equal for t_1 and t_2. This condition corresponds to three variables (x_{C1}, x_{C2}, Q) and two equations (the fitting parameter for p- and n-type n-SiO_x samples, see Figure 13) so, to be satisfied, Q and x_{C1} are assumed constant (but different for p- and n-type) and x_{C1} is arbitrarily fixed to $\frac{1}{2} \cdot t_1$. In other words, Q remains constant for all thicknesses, but it changes its position x_C within the oxide.

Table 6. Fitting parameters of the WF(N) data[d]

		p	n
x_{C1}	nm	0.485	0.485
x_{C2}	nm	0.484	0.485
Q	$\times 10^{13}$ cm^{-2}	(1.82±0.04)	(1.83±0.04)

sgn(eQ)		+	+
w	nm	(3.0±0.3)	(1.3±0.1)
sgn(eNw)		–	+

[d] Fitting parameters obtained fitting the WF data in Figure 12 with Equation 19 and fixing $x_{C1} = ½·t_1$.

Within the experimental errors, the effective sheet charge density in the oxide Q (positive sign, holes) is constant for both dopant type (see Table 6) and in agreement with the literature where it runs from ≈ $9·10^{-11}$ to ≈ $3·10^{-13}$ cm^{-2}.[178–180] The position x_{C2} is slightly reduced or it remains in the same position of the arbitrarily fixed x_{C1}, so Q remains close to the Si/n-SiO_x interface even though the thickness is increased, as reported by Hattori.[141] This result agrees with the XPS results for which an increase in thickness corresponds to an increasing percentage of the more (electronic) stable SiO_2 (cp. Section 3.6). As expected, the width of the depletion layer w is small (in the nm range) because the charge exchange between the crystalline Si substrate and the amorphous n-SiO_x is much less facilitated than a p-n junction where w ≈ 1µm.[181] The sign of the depletion region (minus and plus for p- and n-type, respectively) reflects the presence of charges with opposite sign at the oxide surface, possibly due to the –OH functional groups and their interaction with the airborne contaminations or the Si-O-Si groups (cp. to Section 3.3).[182,183] For the p-type n-SiO_x samples, the oxide surface charges are positive and they shift bands downwards towards a higher depletion. In the n-type ones, the negative charges on the oxide surface compensate the positive interfacial charge and shifts the bands upwards towards depletion rather than accumulation (see Figure 3 of Ref. [163]). Accordingly, w is larger in p-type n-SiO_x samples rather than in the n-type ones (see Table 6).

4. DISCUSSION

Amongst the others, the surface energy γ_S of the n-SiO_x samples merits a particular consideration. As proved in Section 3.1, γ_S vs. N is reproducible regardless of the chemical history of the n-SiO_x samples. This point is pivotal to contest the statement marking the n-SiO_x as irreproducible. Both the growth[149,184] and the surface[111,113] of n-SiO_x depend, in principle, on the airborne contaminants; so, they should be different for different VOC. On the contrary, the reproducibility of γ_S vs. N experiments proved that γ_S is independent on the presence of VOC whereas the dependence on N is preserved.

As proved in a similar experiment,[185] the SiO_2 over layer starts to grow after two weeks of clean room air exposure. The initial Si surface after HF etching terminates with –H groups that, in time, form –OH and Si-O-Si functional groups at the SiO_2/air interface. Both functional groups modulate the charge distribution of the n-SiO_x surface; the Si-O-Si groups by changing their bond angle along time,[185,186] and the –OH groups though their natural polarity.

In view of the results described in Section 3.3, γ_S shows a maximum at N ≈ $2.1·10^{15}$ cm^{-3} for which the concentration of the –OH groups are maximal (highest Θ, tie in Figure 6c) and the one of Si-O-Si groups is minimal (lowest Θ, cross in Figure 6c). Thus, the highest concentration of the –OH groups increase γ_S^p and decreases γ_S^d whereas the lowest concentration of the Si-O-Si groups increases both γ_S^p and γ_S^d. For the additivity introduced by Fowkes,[17] γ_S has its maximum of ≈ 50 dyn·cm^{-1} at N ≈ $2.1·10^{15}$ cm^{-3} (Figure 2a), where this maximum is slightly reduced by the reduction of γ_S^d due to the highest concentration of the –OH groups (Figure 6c). On the other hand, the concurrent contribution of the –OH and Si-O-Si groups to γ_S^d makes it constant and independent of N.

As –OH groups are polar in nature, the n-SiO_x surface should be hydrophilic,[187] as it actually is for most of "as received" n-SiO_x samples and all the regrown ones. Such groups are also reactive, i.e. able to interact with molecules, and thus VOC absorbs immediately on the n-SiO_x surface for equilibrating it. All the n-SiO_x samples reported herein are less hydrophilic than the clean SiO_2,[87,91,92] confirming that VOC are adsorbed on the surface for all samples (see rendering in Figure 14a).

Despite to the presence of adsorbed VOC, the measured polar component of the surface energy, γ_S^p, increases, as expected,[188] for increasing surface density of the –OH groups (cp. Figure 6c to Figure 2b and 3b). This behavior suggests that the polarity of –OH groups is only weakened by the adsorbed VOC but not cancelled.

At the opposite, γ_S^p is reduced for increasing Si-O-Si density.[189] The combination of the opposite effects of –OH and Si-O-Si groups on γ_S^p explains peaks in Figure 2b and 3b.

Regarding the measured dispersive component, γ_S^d, it increases (decreases) with decreasing (increasing) concentration of the Si-O-Si (–OH) groups.[190,191] On the basis of this latter statement, the –OH concentrations on n-SiO_x depends on N in the initial period of the oxide growth (at most in the first three weeks) in which γ_S^d shows a minimum (Figure 3c). Thereafter, γ_S^d stabilizes within (at least) one year and the N dependence is lost (Figure 2c).

On the basis of the aforementioned arguments, the n-SiO_x surface seems consistent with a solid surface mosaic of the two regions,[106] one of relatively low, the other of relatively high surface energy due to Si-O-Si (and SiO_2) and contaminated –OH groups, respectively (see red and green areas in the sketch of Figure 14b). The local contact angle depends on the surface energy of the region with which the liquid is in contact. Therefore, the static contact angle can vary, and the surface gives rise to hysteresis. This scheme is similar to the chemical heterogeneous surface described by the Cassie-Baxter wetting.[192]

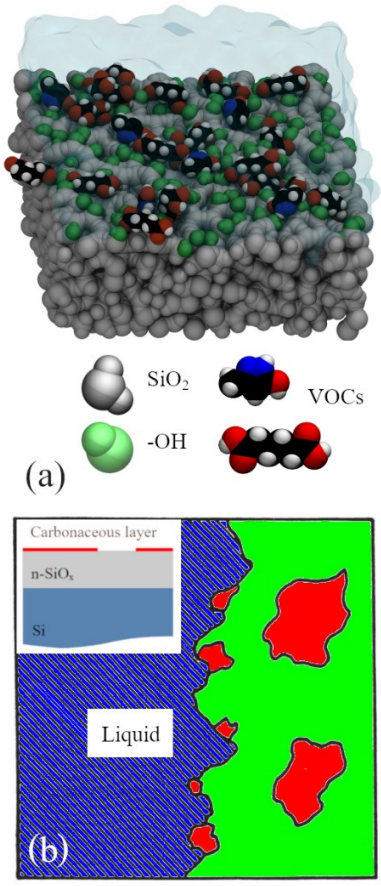

Figure 14. Sketches of the n-SiO_x surface with heterogeneous chemical regions. (a) Rendering of a silicon oxide (silica) surface under typical experimental conditions (RH ≈ 60 % with physisorbed VOC molecules).[193] Grey: SiO_2 bulk; Green: -OH groups on the silica surface; Black/White/Red/Blue: carbon, hydrogen, oxygen, nitrogen atoms belonging to VOC molecules (for instance, Adipic Acid and 3-Methyl-5-pyrazolone as reported in Ref. [147]) physisorbed on the surface; Cyan: isosurface representing a layer of physisorbed water molecules (≈1.5 nm thick); (b) Top view of the possible configuration of the liquid drop (blue area) pinned to heterogeneous superficial regions due to a different chemistry. For instance, heterogeneity could comprise regions with relatively low (green area, Si-O-Si) and relatively high (red regions, contaminated –OH groups) surface energy. Inset: Cross-section of a n-SiO_x sample with a carbonaceous layer deposited on the native oxide due to the airborne contaminations (the oxide and carbonaceous layer thicknesses in the figure are proportional).;

Beyond the chemical heterogeneity of the surface, its roughness affects γ_S.[135] Contrarily to the ordinary evidence, i.e. the larger is the roughness the higher is γ_S, the surface energy is larger where the surface is smoother (see Section 3.4). This apparently contradictory result depends on the concentration of the –OH groups, that is highest for the smoothest surface. In other words, the surface roughness changes are so small that γ_S is mainly driven by the –OH groups.[194]

The contact angle θ of a characterization liquid (water in the reference) on a SiO_2 surface (thermal SiO_2) depends also strongly on the oxide thickness t. [195] Specifically, cos θ increases linearly for increasing t (up to 2 nm) showing a surface wettability evolving from less ($\theta \to \pi/2$) to more hydrophilic ($\theta \to 0$). Such a θ variation can be ascribed to the structure or composition of the oxide. Combining the XPS (Section 3.6) and thickness data (Section 3.5), this hypothesis is also confirmed for the n-SiO_x. The thickness t changes abruptly around $N \approx 10^{15}$ cm^{-3} (Figure 10), where Si^{3+} and Si^{4+} densities are in (or close to) their minima. Concurrently, the monotonic increase in t suggests a structure of the Si intermediate-oxidation states dependent on N because, for instance, the minimum thickness t = 0.9 nm at $N \approx 2 \cdot 10^{13}$ cm^{-3} has relatively high values of both the Si^{3+} and Si^{4+} densities. In other words, the Λ_i percentages in the n-SiO_x are not proportionally distributed to the thickness t as proposed by Seah for the thermal SiO_2.[151,196] This picture makes the t measurements of n-SiO_x more complex than the thermal SiO_2 ones.

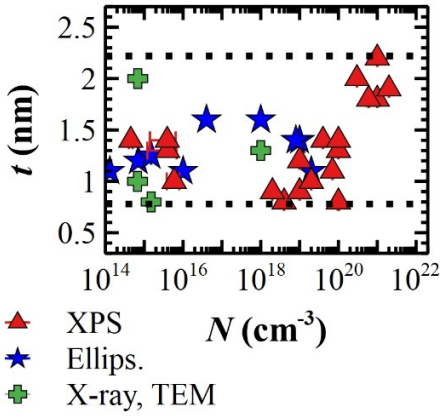

Figure 15. Plot of the thickness data collected from several references (see citations in the main text) vs. N for n-SiO_x grown on Si (100) substrates. The values were obtained with XPS (red triangles), ellipsometry (blue stars) or other techniques (green cross).

The thickness values obtained are consistent with many studies using the same (Ellipsometry and XPS)[97,197–200] or other (Atom Probe and Transmission Electron Microscopy) [201–204] techniques. As shown in Figure 15, t is included in the interval [0.75, 2.2] nm (see dotted lines), like the range obtained in this work. Notably, thicknesses obtained by Wolkenberg's[7] by SE (blue stars) plotted vs. N show a transition region around $N \approx 10^{16}$ cm^{-3}, similar to our findings (see Figure 10). For the XPS data (red triangles), this transition region shifts to $N \approx 10^{20}$ cm^{-3}, in rough agreement to Figure 12 (only one thickness at $N \approx 6.2 \cdot 10^{19}$ cm^{-3}). This shift is ascribable to the model adopted for evaluating the thickness calculated from the XPS data that is constructed for thermal SiO_2. As confirmed by the ellipsometric measurements, the transition region, and so its chemical composition and structure, is markedly different between n-SiO_x and thermal SiO_2.[205] The n-SiO_x thickness data evaluated with ellipsometry are therefore more robust and reliable although specific attention to some technical aspects is needed. As previously mentioned, the thickness values obtained by ellipsometry are dependent on the model adopted to describe the n-SiO_x. The one described herein is feasible, yet simple: three layers were used to describe the n-SiO_x sample, one of

them is the water layer absorbed on the n-SiO_x surface (see Figure 1). Although there is consensus on both the structure of the water layer on SiO_2,[72] and its evolution for increasing RH,[73] there is not on its total thickness[206] and the thickness of a single monolayer of water (experimentally,[207] 0.18 nm, and theoretically,[208] 0.28 nm). At RH ≈ 65 %, the number of water monolayer spans from 2.5[72] to 4.5[73] therefore the total thickness of the adsorbed water can span roughly from 0.4 to 1.2 nm. By using an average value of 0.8 nm, the n-SiO_x thickness t obtained by ellipsometric measurements is increased by 0.55 nm, independently to N. In simple terms, the change of the water layer thickness causes an offset of the whole set of data shown in Figure 10. The composition of the n-SiO_x (bulk) layer might be critical for the model. To test it, the Si concentration (see Table 3) was varied from 0 % to 50 %, returning a t changes of ± 0.13 nm with respect to the thickness obtained at 25 % (see Table 4). Once again, this is independent to N and also the Si concentration at 25 % shows the minimum χ^2 in data fitting, thus corroborating the composition adopted herein

Lastly, the electrical charges are considered. As obtained in Section 3.7, negative and positive charges, Q_S, are present on the outer surface of n-SiO_x due to silanols (see Table 6), whereas positive fixed charges, Q, are present within the oxide. The effect of Q_S on the surface wettability is included in the effect of the –OH and Si-O-Si groups presented in Section 3.3, while the one of fixed charges has to be investigated. As proved by Stoneham *et al.*,[101] fixed charges change θ (free of charges) to θ_C (with charges) and, in particular, θ_C is reduced with increasing surface potential (i.e. $\theta > \theta_{C1} > \theta_{C2}$ for $0 < V(\theta_{C1}) < V(\theta_{C2})$).[209] If one assumes that charges only can affect the liquid–vapor surface energy γ_{SL}, charge effects are accounted by the Young–Lippmann equation:[210]

$$\cos\theta_C = \cos\theta + \frac{\Delta\gamma_C}{\gamma_{LV}} \qquad (20)$$

where the contact angle θ of the "ideal" charge-free oxide changes to θ_C arising from the polarization associated with charges in the oxide.[211] Equation 20 must satisfy the condition $\theta > \theta_C$, correspondent to $\cos\theta < \cos\theta_C$, hence $\Delta\gamma_C \cdot \gamma_{SL}^{-1}$ has to be > 0.

Table 7. Relative permittivity and dipole moments of the characterization liquids[e]

Liquid	ε_r	μ
		D
water	80.1	1.87
glycerol	47	2.56
ethylene glycol	37	2.27
dimethyl-formamide	37.71	3.86

[e] Relative permittivity and dipole moment (in Dalton, D) of the characterization liquids as tabulated in Ref. [212].

In the limit of a very thick oxide, a single charge e placed within n-SiO_x at a distance x from the outer surface contributes with a polarization energy $u(x)$ (in V) of the n-SiO_x – liquid system of:

$$u(x) = \frac{e}{4 \cdot x \cdot \varepsilon_{ox}} \left(\frac{\varepsilon_{ox} - \varepsilon_L}{\varepsilon_{ox} + \varepsilon_L} - \frac{\varepsilon_{ox} - \varepsilon_{air}}{\varepsilon_{ox} + \varepsilon_{air}} \right) \qquad (21)$$

where $\varepsilon_L = \varepsilon_0 \cdot \varepsilon_r$ (in F·cm^{-1}) is the vacuum permittivity ε_0 times the relative permittivity of the characterization liquids and $\varepsilon_{air} = \varepsilon_0$ because ε_r for air is about 1. Based on the relative permittivity of the characterization liquids reported in the literature (see Table 7), the term in brackets does not largely contribute to $u(x)$ because it varies solely of the 6 % passing from water to dimethylformamide. From now on, water is taken as the test liquid for calculations and the term in brackets is thus – 1.50. The limit of a very thick oxide corresponds to a minimum oxide thickness t_{sat} for which the fixed charge Q in the oxide becomes constant to Q_{sat} (saturation region). As proved by Wolkenberg *et al.*,[213] t_{sat} and Q_{sat} depend on N with the lowest t_{sat} at ≈ 300 Å for the highest $Q_{sat} \approx 2 \cdot 10^{12}$ cm^{-2} and the highest N. With decreasing N, t_{sat} progressively increases, while Q_{sat} progressively decreases.

To calculate $u(x)$ in the limit of a very thick oxide layer, the charge e is placed arbitrarily in the position $½ \cdot t_{sat}$ from the outer surface (like in Section 3.7). The function $u(x)$ for t_{sat} > 300 Å, $u(½ \cdot t_{sat})$, is ≈ $u(\infty)$ for an oxide layer infinitely thick because $u(x) \sim x^{-1}$ diverges very slowly for $x \to \infty$. As calculated from Equation 21, $u(½ \cdot t_{sat})$ is 0.116 V and, as reported by Stoneham *et al.*,[101] $\Delta\gamma_C(\infty) \approx \Delta\gamma_C(½ \cdot t_{sat}) = e \cdot Q_{sat} \cdot u(½ \cdot t_{sat})$ that, for $Q_{sat} \approx 2 \cdot 10^{12}$ cm^{-2}, results $-0.37 \cdot 10^{-7}$ J·cm^{-2} = – 0.37 erg·cm^{-2} = – 0.37 dyn·cm^{-1}.

For an ultra-thin oxide layer (t < 50 Å), like the n-SiO_x samples, Stoneham *et al.* proposed a simple empirical form for $\Delta\gamma_C(t)$ referred to $\Delta\gamma_C(\infty)$ for a very thick oxide layer:[101]

$$\frac{\Delta\gamma_C(t)}{\Delta\gamma_C(\infty)} = 1 - 0.7\frac{x_C}{t} \qquad (22)$$

where the surface energy change $\Delta\gamma_C$, due to an effective sheet charge density Q (C·cm^{-2}), is related to the surface energy change for a very thick oxide layer $\Delta\gamma_C(\infty)$. Like in Section 3.7, Q is centered at a plane a distance x_C and calculated integrating a charge density ρ_{ox} which is described by a delta Dirac function at x_C: $Q\,\delta(x - x_C)$, but x_C is referred to the outer surface rather than the n-SiO_x/Si interface. In view of this, Equation 22 is conveniently referred to the n-SiO_x/Si interface:

$$\Delta\gamma_C(t) = \Delta\gamma_C(\infty)\left[1 - 0.7\frac{(t - x_C)}{t}\right] = \Delta\gamma_C(\infty)\left[0.3 + 0.7\frac{x_C}{t}\right] \qquad (23)$$

Using both water as the characterization liquid (γ_{LV} = 72.8 dyn·cm^{-1}) and the data of Table 6, the charge contribution $\Delta\gamma_C/\gamma_{LV}$ is – 0.0033 and – 0.0022 for $x_{C1} \cdot t_1^{-1} = 0.5$ and $x_{C2} \cdot t_2^{-1} = 0.27$, respectively. The minus sign remains because Q is positive (see Table 6). Using Equation 20, $\cos\theta_{C1} < \cos\theta_{C2}$ where θ_{C1} and θ_{C2} are referred to the charge Q in the positions x_{C1} and x_{C2} for thicknesses t_1 and t_2. Thus, $\theta_{C1} > \theta_{C2}$ and hence a thinner n-SiO_x with higher charge should increase the contact angle θ. In contrast to the literature,[209] this result reveals that surface charges Q_S, determined by the –OH groups, give the main electrostatic contribution to θ whereas Q reduces this contribution. Stoneham *et al.*[101] have also evaluated Q from contact angle data collected from Williams *et al.* work[195] reporting a value of Q equal to

a few units of 10^{13} cm^{-2}, in agreement to the results reported in Table 6.

In summary, the surface energy γ_S presents a peak around $N \approx 2.1 \cdot 10^{15}$ cm^{-3} because: i) the chemical and physical properties of the n-SiO_x samples present an abrupt chemical-physical change (thickness and some Si intermediate-oxidation states); ii) the –OH groups concentration and some other Si intermediate-oxidation states have maxima. The electrostatic charges may also contribute, while the changes in surface roughness do not.

5. CONCLUSIONS

Herein, we have demonstrated that the chemical-physical properties of the native silicon oxide layers (n-SiO_x) can be controlled via doping of the Si substrate. Si wafers with N increasing from $\approx 10^{13}$ to $\approx 10^{19}$ cm^{-3}, covered with a n-SiO_x grown in the clean room after production, have been analyzed using different techniques. For a critical level $N \approx 2.1 \cdot 10^{15}$ cm^{-3}, all the properties present either an abrupt change or a maximum. These findings are fully reproducible after oxide removal and regrowth in clean room air, thus giving the same chemical history to n-SiO_x samples. Additional experiments are necessary to: i) clarify the nature of this critical N value, although some literature results suggest a correlation among $N \approx 10^{15}$ cm^{-3}, the chemical stoichiometry[214] and/or the oxygen concentration[88] of the n-SiO_x; ii) elucidate the role of the crystallographic orientation of the Si substrate; and iii) investigate if the method to fabricate wafers (CZ or FZ) affects the n-SiO_x. These queries might be discerned by following the oxide growth step by step for all N.[97,215,216]

Airborne contaminants, adsorbed on n-SiO_x surfaces when exposed to air, are crucial to equilibrate a portion of–OH groups. Nowadays, their presence is observed through Contact Angle measurements deviations in water contact angle, hysteresis measurements, or as a carbonaceous layer atop the n-SiO_x by XPS. Scanning probe microscopy measurements might be useful to visualize them directly, as chemical heterogeneous regions, or indirectly, through morphological analysis.[76,217,218]

The results reported in this work confirm that the n-SiO_x is a "non-innocent surface", as defined in the literature.[219] Such results are also potentially important for experiments where the n-SiO_x is used as low-interacting substrate, like aggregation phenomena of molecules or nanometric objects. As previously reported,[220] the surface molecular diffusion is driven by the interfacial properties of the substrate and so it can be systematically modulated by using a set of n-SiO_x with increasing N. A few examples of aggregation phenomena adopting this strategy are reported in the literature: few of them use substrates with completely different chemical-physical properties,[221] but others follow this way tuning finely the molecular aggregation through the properties of the substrate.[23,24,76,222]

ASSOCIATED CONTENT

Supporting Information. Statistical measurements of the contact angle θ; Surface energy of n-SiOx with different characterization liquids; Morphological analysis of native silicon oxides, Skewness and Kurtosis measurements of height distributions extracted from n-SiO_x topographic images; Step-like trend of thickness t vs. N; XPS spectra. This material is available free of charge via the Internet at http://pubs.acs.org.

AUTHOR INFORMATION

Corresponding Author

* **E-mail:** cristiano.albonetti@cnr.it

Present Addresses

† Via Selice Provinciale 17/A, 40026, Imola, Italy.

Author Contributions

The manuscript was written through contributions of all authors. All authors have given approval to the final version of the manuscript

Funding Sources

The work was supported by EC projects FP7 ONE-P large-scale project n° 212311 and EU-STREP ForceTool (NMP4-CT-2004-STRP 013684).

ACKNOWLEDGMENT

The authors wish to thank Claudio Della Volpe and Stefano Siboni for useful discussions and suggestions on contact angle measurements and data interpretations, Francesca Leonardi for contact angle measurements reported in the Supplementary Materials, Federico Prescimone for the clean room access, Fabiola Liscio for X-ray diffraction measurements useful to determine the crystallographic orientations of some n-SiO_x samples, Giampiero Ruani for IR measurements, Maria Otello Roscioni for Figure 14b, and Franco Dinelli for proofreading the manuscript. SPM and SEM images were elaborated with the software Gwyddion,[223] data were analysed by the GNU General Public Licensed Software QtiPlot and figures are prepared by the GNU General Public Licensed Software Veusz. AFM and SEM images, Contact Angle and Ellispometric measurements were collected in the SPM@ISMN facility.

ABBREVIATIONS

n-SiOx, native silicon oxide; XPS, X-ray photoemission spectroscopy; TD, Thermal desorption; AFM, Atomic Force Microscopy; KP, Kelvin Probe; CZ, Czochralski method; FZ, floating zone method; O-W, Owens and Wendt method; RGA, Residual Gas Analyser; ToF-SIMS, Time-of-Flight Secondary Ion Mass Spectrometry; SAMs, Self-Assembly Monolayers; TFOCS, Tridecafluoro-1,1,2,2-tetrahydrooctyl-1-trichlorosilane; HHCF, Height-Height Correlation Function; UHV, ultrahigh vacuum; H, contact angle hysteresis; VOC, Volatile Organic Compounds.

REFERENCES

(1) Liu, Y. J.; Yu, H. Z. Alkyl Monolayer Passivated Metal-Semiconductor Diodes: 2:** Comparison with Native Silicon Oxide. *ChemPhysChem* **2003**, *4* (4), 335–342. https://doi.org/10.1002/cphc.200390059.

(2) Chin, A.; Lin, B. C.; Chen, W. J.; Lin, Y. B.; Tsai, C. The Effect of Native Oxide on Thin Gate Oxide Integrity. *IEEE Electron Device Lett.* **1998**, *19* (11), 426–428. https://doi.org/10.1109/55.728901.

(3) Kern, W. Overview and Evolution of Silicon Wafer Cleaning Technology. In *Handbook of Silicon Wafer Cleaning Technology*; Reinhardt, K. A., Kern, W. B. T.-H. of S. W. C. T. (Third E., Eds.; William Andrew Publishing, 2018; pp 3–85. https://doi.org/10.1016/B978-0-323-51084-4.00001-0.

(4) Silicon/Electrolyte Interface. In *Electrochemistry of Silicon and Its Oxide*; Zhang, X. G., Ed.; Springer US: Boston, MA, 2005; pp 45–90. https://doi.org/10.1007/0-306-47921-4_2.

(5) Ying, W. B.; Mizokawa, Y.; Tanahashi, K.; Kamiura, Y.; Iida, M.; Kawamoto, K.; Yang, W. Y.; Yingag, W. B.; Tanahashia, K.; Kamiuraa, Y.; Iidab, M.; Yangc, W. Y. Evaluation of the Initial Oxidation of Heavily Phosphorus Doped Silicon Surfaces Using Angle-Dependent X-Ray Photoelectron Spectroscopy. *Thin Solid Films* **1999**, *343–344*, 393–396. https://doi.org/10.1016/S0040-6090(99)00118-2.

(6) Ying, W. B.; Mizokawa, Y.; Kamiura, Y.; Kawamoto, K.; Yang, W. Y. The Chemical Composition Changes of Silicon and Phosphorus in the Process of Native Oxide Formation of Heavily Phosphorus Doped Silicon. *Appl. Surf. Sci.* **2001**, *181* (1–2), 1–14. https://doi.org/10.1016/S0169-4332(01)00202-1.

(7) Wolkenberg, A. A Mechanism for the Effect of Doping on the Silicon Native Oxide Thickness. *Phys. Status Solidi* **1983**, *79* (1), 313–322. https://doi.org/10.1002/pssa.2210790135.

(8) Freiberg Instruments. Resistance measurements on wafers and bricks https://www.freiberginstruments.com/upcdmdp/applications/resistance-measurements-on-wafers-and-bricks.html.

(9) ECEn IMMERSE Web Team. Resistivity & Mobility Calculator http://www.cleanroom.byu.edu/ResistivityCal.phtml.

(10) Ehrstein, J. R.; Croarkin, C. M. Standard Reference Materials: The Certification of 100 Mm Diameter Silicon Resistivity SRMs 2541 through 2547 Using Dual-Configuration Four-Point Probe Measurements. **1999**.

(11) Araki, N. Influence of Electrostatic Charge on Recombination Lifetime and Native Oxide Growth on HF-Treated Silicon Wafers. *Jpn. J. Appl. Phys.* **2009**, *48* (1). https://doi.org/10.1143/JJAP.48.011201.

(12) Okada, C.; Kobayashi, H.; Takahashi, I.; Ryuta, J.; Shingyouji, T. Growth of Native Oxide and Accumulation of Organic Matter on Bare Si Wafer in Air. *Jpn. J. Appl. Phys.* **1993**, *32* (8 A), L 1031-L 1033. https://doi.org/10.1143/JJAP.32.L1031.

(13) Stanford Nanofabrication Facility. Cleaving Wafers and Substrates https://www.youtube.com/watch?v=IRoIXjxIcBQ.

(14) Sugimoto, F.; Okamura, S. Adsorption Behavior of Organic Contaminants on a Silicon Wafer Surface. *J. Electrochem. Soc.* **1999**, *146* (7), 2725–2729. https://doi.org/10.1149/1.1392000.

(15) Lizon, J. L.; Deiries, S. Cleaning of Extremely Sensitive Optical Surfaces. In *Advances in Optical and Mechanical Technologies for Telescopes and Instrumentation*; 2014; Vol. 9151, p 91515A. https://doi.org/10.1117/12.2054694.

(16) Owens, D. K.; Wendt, R. C. Estimation of the Surface Free Energy of Polymers. *J. Appl. Polym. Sci.* **1969**, *13* (8), 1741–1747. https://doi.org/https://doi.org/10.1002/app.1969.070130815.

(17) Fowkes, F. M. Additivity of Intermolecular Forces At Interfaces. I. Determination of the Contribution To Surface and Interfacial Tensions of Dispersion Forces in Various Liquids 1 . *J. Phys. Chem.* **1963**, *67* (12), 2538–2541. https://doi.org/10.1021/j100806a008.

(18) Drelich, J. W.; Boinovich, L.; Chibowski, E.; Della Volpe, C.; Hołysz, L.; Marmur, A.; Siboni, S. Contact Angles: History of over 200 Years of Open Questions. *Surf. Innov.* **2020**, *8* (1–2), 3–27. https://doi.org/10.1680/jsuin.19.00007.

(19) Boyd, G. E.; Livingston, H. K. Adsorption and the Energy Changes at Crystalline Solid Surfaces. *J. Am. Chem. Soc.* **1942**, *64* (10), 2383–2388. https://doi.org/10.1021/ja01262a047.

(20) Schlangen, L. J. M.; Koopal, L. K.; Cohen Stuart, M. A.; Lyklema, J. Wettability: Thermodynamic Relationships between Vapour Adsorption and Wetting. *Colloids Surfaces A Physicochem. Eng. Asp.* **1994**, *89* (2–3), 157–167. https://doi.org/10.1016/0927-7757(94)80115-0.

(21) Cwikel, D.; Zhao, Q.; Liu, C.; Su, X.; Marmur, A. Comparing Contact Angle Measurements and Surface Tension Assessments of Solid Surfaces. *Langmuir* **2010**, *26* (19), 15289–15294. https://doi.org/10.1021/la1020252.

(22) ELYT. A guide to surface texture parameters https://www.ossila.com/en-eu/pages/a-guide-to-surface-energy.

(23) Koch, N.; Zojer, E.; Rajagopal, A.; Ghjisen, J.; Johnson, R. L.; Leising, G.; Pireaux, J. J. Electronic Properties of the Interfaces between the Wide Bandgap Organic Semiconductor Para-Sexiphenyl and Samarium. *Adv. Funtional Mater.* **2001**, *11* (1), 51–58. https://doi.org/10.1002/1616-3028(200102)11:1<51::AID-ADFM51>3.0.CO;2-Q.

(24) Verlaak, S.; Steudel, S.; Heremans, P.; Heremans, P.; Janssen, D.; Janssen, D.; Deleuze, M. S. Nucleation of Organic Semiconductors on Inert Substrates. *Phys. Rev. B* **2003**, *68* (19), 195409. https://doi.org/10.1103/PhysRevB.68.195409.

(25) Büchner, C.; Heyde, M.; Freund, H. J. Transfer of 2D Silica Films. In *Encyclopedia of Interfacial Chemistry: Surface Science and Electrochemistry*; Wandelt, K. B. T.-E. of I. C., Ed.; Elsevier: Oxford, 2018; pp 360–366. https://doi.org/10.1016/B978-0-12-409547-2.14171-X.

(26) Radelczuk, H.; Hołysz, L.; Chibowski, E. Comparison of the Lifshitz-van Der Waals/Acid-Base and Contact Angle Hysteresis Approaches for Determination of Solid Surface Free Energy. *J. Adhes. Sci. Technol.* **2002**, *16* (12), 1547–1568. https://doi.org/10.1163/15685610260255215.

(27) Van Oss, C. J.; Giese, R. F.; Wu, W. On the Predominant Electron-Donicity of Polar Solid Surfaces. *J. Adhes.* **1997**, *63* (1–3), 71–88. https://doi.org/10.1080/00218469708015214.

(28) Louisiana State University. Surface Tension https://macro.lsu.edu/HowTo/solvents/Surface Tension.htm.

(29) ACCU DYNE TEST. Surface Tension Components and Molecular Weight of Selected Liquids https://www.accudynetest.com/surface_tension_table.html.

(30) Dann, J. R. Forces Involved in the Adhesive Process: I. Critical Surface Tensions of Polymeric Solids as Determined with Polar Liquids. *J. Colloid Interface Sci.* **1970**, *32* (2), 302–320. https://doi.org/https://doi.org/10.1016/0021-9797(70)90054-8.

(31) Hoffman, A. S. Contact Angle Lecture https://www.yumpu.com/en/document/view/11872520/contact-angle-lecture-uweb.

(32) Koenhen, D. M.; Smolders, C. A. The Determination of Solubility Parameters of Solvents and Polymers by Means of Correlations with Other Physical Quantities. *J. Appl. Polym. Sci.* **1975**, *19* (4), 1163–1179. https://doi.org/https://doi.org/10.1002/app.1975.070190423.

(33) Florea-Spiroiu, M.; Olteanu, M.; Stanescu, V.; Nechifor, G. Surface Tension Components of Plasma Treated Polysulphone Membranes. *Analele Univ. Nii din Bucuresti–Chimie, Anul XVII (serie noua)* **2008**, *2*, 13–18.

(34) Rulison, C. So you want to measure surface energy? http://www.surfchem.co.kr/newapplications/pdf/15.pdf.

(35) Vicente, C. M. .; André, P. S.; Ferreira, R. A. S. Simple Measurement of Surface Free Energy Using a Web Cam. *Rev. Bras. Ensino Física* **2012**, *34* (3), 1–5. https://doi.org/10.1590/S1806-11172012000300012.

(36) Della Ciana, M. Studio Della Correlazione Tra Il Drogaggio Del Silicio e l'energia Superficiale Del Suo Ossido Nativo, Alma Mater Studiorum - Università di Bologna, 2015.

(37) Li, D.; Neumann, A. W. Equation of State for Interfacial Tensions of Solid-Liquid Systems. *Adv. Colloid Interface Sci.* **1992**, *39* (C), 299–345. https://doi.org/10.1016/0001-8686(92)80064-5.

(38) Durkee, J. B. Cleaning with Solvents. In *Developments in Surface Contamination and Cleaning: Fundamentals and Applied Aspects*; Kohli, R., Mittal, K. L. B. T.-D. in S. C. and C., Eds.; William Andrew Publishing: Norwich, NY, 2007; pp 759–871. https://doi.org/10.1016/B978-081551555-5.50017-4.

(39) Saga, K.; Hattori, T. Identification and Removal of Trace Organic Contamination on Silicon Wafers Stared in Plastic Boxes. *J. Electrochem. Soc.* **1996**, *143* (10), 3279–3284.

https://doi.org/10.1149/1.1837198.
(40) Gao, L.; McCarthy, T. J. Contact Angle Hysteresis Explained. *Langmuir* **2006**, *22* (14), 6234–6237. https://doi.org/10.1021/la060254j.
(41) Yuan, Y.; Lee, T. R. Contact Angle and Wetting Properties. In *Springer Series in Surface Sciences*; Bracco, G., Holst, B., Eds.; Springer Berlin Heidelberg: Berlin, Heidelberg, 2013; Vol. 51, pp 3–34. https://doi.org/10.1007/978-3-642-34243-1_1.
(42) Extrand, C. W.; Kumagai, Y. Liquid Drops on an Inclined Plane: The Relation between Contact Angles, Drop Shape, and Retentive Force. *J. Colloid Interface Sci.* **1995**, *170* (2), 515–521. https://doi.org/10.1006/jcis.1995.1130.
(43) Extrand, C. W. Contact Angles and Hysteresis on Surfaces with Chemically Heterogeneous Islands. *Langmuir* **2003**, *19* (9), 3793–3796. https://doi.org/10.1021/la0268350.
(44) Joanny, J. F.; De Gennes, P. G. A Model for Contact Angle Hysteresis. *J. Chem. Phys.* **1984**, *81* (1), 552–562. https://doi.org/10.1063/1.447337.
(45) Extrand, C. W.; Kumagai, Y. An Experimental Study of Contracted Angle Hysteresis. *J. Colloid Interface Sci.* **1997**, *191* (2), 378–383. https://doi.org/10.1006/jcis.1997.4935.
(46) Danel, A.; Rochat, N.; Olivier, M.; Roche, A.; Tardif, F. Dry Cleaning of Organic Contamination on Silicon Wafers Using Rapid Optical Surface Treatment. *Solid State Phenom.* **2001**, *76–77*, 59–62. https://doi.org/10.4028/www.scientific.net/SSP.76-77.59.
(47) Tsai, C.-L.; Roman, P.; Wu, C.-T.; Pantano, C.; Berry, J.; Kamieniecki, E.; Ruzyllo, J. Control of Organic Contamination of Silicon Surfaces Using White Light Illumination in Ambient Air. *J. Electrochem. Soc.* **2003**, *150* (1), G39. https://doi.org/10.1149/1.1527053.
(48) Vidal, A. M.; Papirer, E. Surface Chemistry and Surface Energy of Silicas. In *Colloidal Silica: Fundamentals and Applications*; Advances in Chemistry; American Chemical Society, 2005; Vol. 234, pp 379–384. https://doi.org/10.1201/9781420028706-35.
(49) Jin, J.; Wang, X.; Wick, C. D.; Dang, L. X.; Miller, J. D. Silica Surface States and Their Wetting Characteristics. *Surf. Innov.* **2019**, *8* (3), 145–157. https://doi.org/10.1680/jsuin.19.00053.
(50) Chen, C.; Zhang, N.; Li, W.; Song, Y. Water Contact Angle Dependence with Hydroxyl Functional Groups on Silica Surfaces under CO2 Sequestration Conditions. *Environ. Sci. Technol.* **2015**, *49* (24), 14680–14687. https://doi.org/10.1021/acs.est.5b03646.
(51) Owen, M. J. Siloxane Surface Activity. In *Silicon-Based Polymer Science*; Advances in Chemistry; American Chemical Society, 1989; Vol. 224, pp 705–739. https://doi.org/10.1021/ba-1990-0224.ch040.
(52) Raghu, P.; Rana, N.; Yim, C.; Shero, E.; Shadman, F. Adsorption of Moisture and Organic Contaminants on Hafnium Oxide, Zirconium Oxide, and Silicon Oxide Gate Dielectrics. *J. Electrochem. Soc.* **2003**, *150* (10), F186. https://doi.org/10.1149/1.1605747.
(53) Cusumano, J. A.; Low, M. J. D. Interaction between Surface Hydroxyl Groups and Adsorbed Molecules. III. The Nature of the Adsorbate-Hydroxyl Interaction. *J. Catal.* **1971**, *23* (2), 214–227. https://doi.org/10.1016/0021-9517(71)90043-1.
(54) Miozzo, L.; Yassar, A.; Horowitz, G. Surface Engineering for High Performance Organic Electronic Devices: The Chemical Approach. *J. Mater. Chem.* **2010**, *20* (13), 2513–2538. https://doi.org/10.1039/b922385a.
(55) Hadjiivanov, K. Identification and Characterization of Surface Hydroxyl Groups by Infrared Spectroscopy. In *Advances in Catalysis*; Jentoft, F. C. B. T.-A. in C., Ed.; Academic Press, 2014; Vol. 57, pp 99–318. https://doi.org/10.1016/B978-0-12-800127-1.00002-3.
(56) Qin, D.; Xia, Y.; Whitesides, G. M. Soft Lithography for Micro- and Nanoscale Patterning. *Nat. Protoc.* **2010**, *5* (3), 491–502. https://doi.org/10.1038/nprot.2009.234.
(57) Seah, M. P.; Spencer, S. J. Ultrathin SiO2 on Si. I. Quantifying and Removing Carbonaceous Contamination. *J. Vac. Sci. Technol. A Vacuum, Surfaces, Film.* **2003**, *21* (2), 345–352. https://doi.org/10.1116/1.1535173.
(58) Gong, Y.; Misture, S. T.; Gao, P.; Mellott, N. P. Surface Roughness Measurements Using Power Spectrum Density Analysis with Enhanced Spatial Correlation Length. *J. Phys. Chem. C* **2016**, *120* (39), 22358–22364. https://doi.org/10.1021/acs.jpcc.6b06635.
(59) Bhushan, B. Surface Roughness Analysis and Measurement Techniques. In *Modern Tribology Handbook: Volume One: Principles of Tribology*; CRC press, 2000; pp 49–119. https://doi.org/10.1201/9780849377877-10.
(60) Valle, F.; Brucale, M.; Chiodini, S.; Bystrenova, E.; Albonetti, C. Nanoscale Morphological Analysis of Soft Matter Aggregates with Fractal Dimension Ranging from 1 to 3. *Micron* **2017**, *100*, 60–72. https://doi.org/10.1016/j.micron.2017.04.013.
(61) Jellison, G. E. Examination of Thin SiO2 Films on Si Using Spectroscopic Polarization Modulation Ellipsometry. *J. Appl. Phys.* **1991**, *69* (11), 7627–7634. https://doi.org/10.1063/1.347532.
(62) Herzinger, C. M.; Johs, B.; McGahan, W. A.; Woollam, J. A.; Paulson, W. Ellipsometric Determination of Optical Constants for Silicon and Thermally Grown Silicon Dioxide via a Multi-Sample, Multi-Wavelength, Multi-Angle Investigation. *J. Appl. Phys.* **1998**, *83* (6), 3323–3336. https://doi.org/10.1063/1.367101.
(63) Wang, Y.; Irene, E. A. Consistent Refractive Index Parameters for Ultrathin SiO2 Films. *J. Vac. Sci. Technol. B Microelectron. Nanom. Struct. Process. Meas. Phenom.* **2000**, *18* (1), 279–282. https://doi.org/10.1116/1.591183.
(64) Lai, L.; Hebert, K. J.; Irene, E. A. A Study of the Relationship between Si/SiO2 between Interface Charges and Roughness. *J. Vac. Sci. Technol. B Microelectron. Nanom. Struct. Process. Meas. Phenom.* **1999**, *17* (1), 53–59. https://doi.org/10.1116/1.590516.
(65) Khalilov, U.; Pourtois, G.; Huygh, S.; Van Duin, A. C. T.; Neyts, E. C.; Bogaerts, A. New Mechanism for Oxidation of Native Silicon Oxide. *J. Phys. Chem. C* **2013**, *117* (19), 9819–9825. https://doi.org/10.1021/jp400433u.
(66) Ying, W. B.; Mizokawa, Y.; Kamiura, Y.; Kawamoto, K.; Yang, W. Y. The Chemical Composition Changes of Silicon and Phosphorus in the Process of Native Oxide Formation of Heavily Phosphorus Doped Silicon. *Appl. Surf. Sci.* **2001**, *181* (1–2), 1–14. https://doi.org/10.1016/S0169-4332(01)00202-1.
(67) Khalilov, U.; Pourtois, G.; Van Duin, A. C. T.; Neyts, E. C. On the c -Si| a -SiO 2 Interface in Hyperthermal Si Oxidation at Room Temperature. *J. Phys. Chem. C* **2012**, *116* (41), 21856–21863. https://doi.org/10.1021/jp306920p.
(68) Yano, F.; Hiraoka, A.; Itoga, T.; Kojima, H.; Kanehori, K.; Mitsui, Y. Influence of Ion-Implantation on Native Oxidation of Si in a Clean-Room Atmosphere. *Appl. Surf. Sci.* **1996**, *100–101*, 138–142. https://doi.org/10.1016/0169-4332(96)00274-7.
(69) Beaglehole, D.; Christenson, H. K. Vapor Adsorption on Mica and Silicon: Entropy Effects, Layering, and Surface Forces. *J. Phys. Chem.* **1992**, *96* (8), 3395–3403. https://doi.org/10.1021/j100187a040.
(70) Masteika, V.; Kowal, J.; Braithwaite, N. S. J.; Rogers, T. A Review of Hydrophilic Silicon Wafer Bonding. *ECS J. Solid State Sci. Technol.* **2014**, *3* (4), Q42–Q54. https://doi.org/10.1149/2.007403jss.
(71) Garcia-Caurel, E.; De Martino, A.; Gaston, J. P.; Yan, L. Application of Spectroscopic Ellipsometry and Mueller Ellipsometry to Optical Characterization. *Appl. Spectrosc.* **2013**, *67* (1), 1–21. https://doi.org/10.1366/12-06883.
(72) Asay, D. B.; Kim, S. H. Evolution of the Adsorbed Water Layer Structure on Silicon Oxide at Room Temperature. *J. Phys. Chem. B* **2005**, *109* (35), 16760–16763. https://doi.org/10.1021/jp053042o.
(73) Theillet, P. O.; Pierron, O. N. Quantifying Adsorbed Water Monolayers on Silicon MEMS Resonators Exposed to Humid Environments. *Sensors Actuators, A Phys.* **2011**, *171* (2), 375–380. https://doi.org/10.1016/j.sna.2011.09.002.
(74) Bruggeman, D. A. G. Berechnung Verschiedener Physikalischer Konstanten von Heterogenen Substanzen. I. Dielektrizitätskonstanten Und Leitfähigkeiten Der Mischkörper Aus Isotropen Substanzen. *Ann. Phys.* **1935**, *416*

(8), 665–679. https://doi.org/https://doi.org/10.1002/andp.19354160802.
(75) Klapetek, P.; Necas, D.; Anderson, C. *Gwyddion User Guide*.
(76) Chiodini, S.; Dinelli, F.; Martinez, N. F.; Donati, S.; Albonetti, C. Identification of Ultra-Thin Molecular Layers atop Monolayer Terraces in Sub-Monolayer Organic Films with Scanning Probe Microscopy. *Ultramicroscopy* **2022**, *240*, 113598. https://doi.org/10.1016/j.ultramic.2022.113598.
(77) Hilfiker, J. N.; Sun, J.; Hong, N. Data Analysis BT - Spectroscopic Ellipsometry for Photovoltaics: Volume 1: Fundamental Principles and Solar Cell Characterization; Fujiwara, H., Collins, R. W., Eds.; Springer International Publishing: Cham, 2018; pp 59–88. https://doi.org/10.1007/978-3-319-75377-5_3.
(78) Palik, E. D. *Handbook of Optical Constants of Solids*; Academic Press New York, 1991; Vol. 2 and 3.
(79) Gilliot, M. Errors in Ellipsometry Data Fitting. *Opt. Commun.* **2018**, *427*, 477–484. https://doi.org/https://doi.org/10.1016/j.optcom.2018.07.025.
(80) Walton J; Wincott P; Fairley N; Carrick A. *Peak Fitting with CasaXPS: A Casa Pocket Book* ; Accolyte Science: United Kingdom, 2010.
(81) KP Technology. Scanning Kelvin Probe https://www.kelvinprobe.com/products_info.php?ind=4.
(82) Camp, J. B.; Darling, T. W.; Brown, R. E. Macroscopic Variations of Surface Potentials of Conductors. *J. Appl. Phys.* **1991**, *69* (10), 7126–7129. https://doi.org/10.1063/1.347601.
(83) Huber, S.; Wicinski, M.; Hassel, A. W. Suitability of Various Materials for Probes in Scanning Kelvin Probe Measurements. *Phys. Status Solidi Appl. Mater. Sci.* **2018**, *215* (15), 1700952. https://doi.org/10.1002/pssa.201700952.
(84) Reasenberg, R. D.; Donahue, K. P.; Phillips, J. D. Analysis and Simulation of the Operation of a Kelvin Probe. *Class. Quantum Gravity* **2013**, *30* (12), 125016. https://doi.org/10.1088/0264-9381/30/12/125016.
(85) Seeger, L.; Lobnig, R.; Wicinski, M. New Calibration Method for Kelvin Probe in Changing Humidity Conditions. *J. Electrochem. Soc.* **2022**, *169* (10), 101501. https://doi.org/10.1149/1945-7111/ac8fbc.
(86) Chibowski, E.; Ontiveros-Ortega, A.; Perea-Carpio, R. On the Interpretation of Contact Angle Hysteresis. *J. Adhes. Sci. Technol.* **2002**, *16* (10), 1367–1404. https://doi.org/10.1163/156856102320252859.
(87) Zdziennicka, A.; Szymczyk, K.; Krawczyk, J.; Jańczuk, B. Some Remarks on the Solid Surface Tension Determination from Contact Angle Measurements. *Appl. Surf. Sci.* **2017**, *405*, 88–101. https://doi.org/10.1016/j.apsusc.2017.01.068.
(88) Narayan, S. R.; Day, J. M.; Thinakaran, H. L.; Herbots, N.; Bertram, M. E.; Cornejo, C. E.; Diaz, T. C.; Kavanagh, K. L.; Culbertson, R. J.; Ark, F. J.; Ram, S.; Mangus, M. W.; Islam, R. Comparative Study of Surface Energies of Native Oxides of Si(100) and Si(111) via Three Liquid Contact Angle Analysis. *MRS Adv.* **2018**, *3* (57–58), 3379–3390. https://doi.org/10.1557/adv.2018.473.
(89) Sun, H.; Liu, J.; Gu, P.; Chen, D. Anti-Sticking Treatment for a Nanoimprint Stamp. *Appl. Surf. Sci.* **2008**, *254* (10), 2955–2959. https://doi.org/10.1016/j.apsusc.2007.10.047.
(90) Kawai, A.; Kawakami, J. Characterization of SiO2 Surface Treated by HMDS Vapor and O2 Plasma with AFM Tip. *J. Photopolym. Sci. Technol.* **2003**, *16* (5), 665–668. https://doi.org/10.2494/photopolymer.16.665.
(91) Janssen, D.; De Palma, R.; Verlaak, S.; Heremans, P.; Dehaen, W. Static Solvent Contact Angle Measurements, Surface Free Energy and Wettability Determination of Various Self-Assembled Monolayers on Silicon Dioxide. *Thin Solid Films* **2006**, *515* (4), 1433–1438. https://doi.org/https://doi.org/10.1016/j.tsf.2006.04.006.
(92) Xing, Q.; Herbots, N.; Hart, M.; Bradley, J. D.; Wilkens, B. J.; Sell, D. A.; Sell, C. H.; Kwong, H. M.; Culbertson, R. J.; Whaley, S. D. Ion Beam Analysis of Silicon-Based Surfaces and Correlation with Surface Energy Measurements. *AIP Conf. Proc.* **2011**, *1336* (1), 201–207. https://doi.org/10.1063/1.3586089.
(93) Lo, Y. S.; Huefner, N. D.; Chan, W. S.; Dryden, P.; Hagenhoff, B.; Beebe, T. P. Organic and Inorganic Contamination on Commercial AFM Cantilevers. *Langmuir* **1999**, *15* (19), 6522–6526. https://doi.org/10.1021/la990371x.
(94) Deckert, C. A.; Peters, D. A. Adhesion, Wettability, and Surface Chemistry.; Mittal, K. L., Ed.; Springer US: Boston, MA, 1983; pp 469–498. https://doi.org/10.1007/978-1-4613-3658-7_28.
(95) Iglauer, S.; Salamah, A.; Sarmadivaleh, M.; Liu, K.; Phan, C. Contamination of Silica Surfaces: Impact on Water-CO2-Quartz and Glass Contact Angle Measurements. *Int. J. Greenh. Gas Control* **2014**, *22*, 325–328. https://doi.org/10.1016/j.ijggc.2014.01.006.
(96) Kern, W. Evolution of Silicon Wafer Cleaning Technology. *Proc. - Electrochem. Soc.* **1990**, *90* (9), 3–19. https://doi.org/10.1149/1.2086825.
(97) Morita, M.; Ohmi, T.; Hasegawa, E.; Kawakami, M.; Ohwada, M. Growth of Native Oxide on a Silicon Surface. *J. Appl. Phys.* **1990**, *68* (3), 1272–1281. https://doi.org/10.1063/1.347181.
(98) Hermansson, K.; Lindberg, U.; Hok, B.; Palmskog, G. Wetting Properties of Silicon Surfaces. In *Transducers '91*; 1991; pp 193–196. https://doi.org/10.1109/sensor.1991.148835.
(99) Schaible, M. Empirical Molecular Dynamics Modeling of Silicon and Silicon Dioxide: A Review. *Crit. Rev. Solid State Mater. Sci.* **1999**, *24* (4), 265–323. https://doi.org/10.1080/10408439991329215.
(100) Matsuo, N.; Kawamoto, N.; Aihara, D.; Miyoshi, T. Initial Stage of Adsorption for Organic Carbons and Native Oxide Growth on Si Wafer. *Appl. Surf. Sci.* **2000**, *159*, 41–44. https://doi.org/10.1016/S0169-4332(00)00044-1.
(101) Stoneham, A. M.; Tasker, P. W. The Wetting of Oxide Films on Silicon and the Monitoring of Fixed Charge. *Semicond. Sci. Technol.* **1986**, *1* (1), 93–96. https://doi.org/10.1088/0268-1242/1/1/011.
(102) Habib, S. B.; Gonzalez, E.; Hicks, R. F. Atmospheric Oxygen Plasma Activation of Silicon (100) Surfaces. *J. Vac. Sci. Technol. A Vacuum, Surfaces, Film.* **2010**, *28* (3), 476–485. https://doi.org/10.1116/1.3374738.
(103) Schmitt, M.; Hempelmann, R.; Heib, F. Experimental Investigation of Dynamic Contact Angles on Horizontal and Inclined Surfaces Part I: Flat Silicon Oxide Surfaces. *Zeitschrift fur Phys. Chemie* **2014**, *228* (1), 11–25. https://doi.org/10.1515/zpch-2014-0443.
(104) Lamb, R. N.; Furlong, D. N. Controlled Wettability of Quartz Surfaces. *J. Chem. Soc. Faraday Trans. 1 Phys. Chem. Condens. Phases* **1982**, *78* (1), 61–73. https://doi.org/10.1039/F19827800061.
(105) Thomas, R. R.; Kaufman, F. B.; Kirleis, J. T.; Belsky, R. A. Wettability of Polished Silicon Oxide Surfaces. *J. Electrochem. Soc.* **1996**, *143* (2), 643–648. https://doi.org/10.1149/1.1836494.
(106) Yekta-Fard, M.; Ponter, A. B. Factors Affecting the Wettability of Polymer Surfaces. *J. Adhes. Sci. Technol.* **1992**, *6* (2), 253–277. https://doi.org/10.1163/156856192X00322.
(107) Tarasevich, Y. I. Surface Energy of Oxides and Silicates. *Theor. Exp. Chem.* **2006**, *42* (3), 145–161. https://doi.org/10.1007/s11237-006-0031-6.
(108) Pogorzelski, S. J.; Berezowski, Z.; Rochowski, P.; Szurkowski, J. A Novel Methodology Based on Contact Angle Hysteresis Approach for Surface Changes Monitoring in Model PMMA-Corega Tabs System. *Appl. Surf. Sci.* **2012**, *258* (8), 3652–3658. https://doi.org/10.1016/j.apsusc.2011.11.132.
(109) Juneja, H. Removal of Adsorbed Moisture and Organics from Surfaces and Nanostructures in Semiconductor Manufacturing, The University of Arizona., 2008.
(110) Poleunis, C.; Delcorte, A.; Bertrand, P. Determination of Organic Contaminations on Si Wafer Surfaces by Static ToF-SIMS: Improvement of the Detection Limit with C 60+ Primary Ions. *Appl. Surf. Sci.* **2006**, *252* (19), 7258–7261. https://doi.org/10.1016/j.apsusc.2006.02.267.
(111) Karen, A.; Man, N.; Shibamori, T.; Takahashi, K. TOF-SIMS Characterization of Industrial Materials: From Silicon Wafer to Polymer. *Appl. Surf. Sci.* **2003**, *203–204*, 541–546.

https://doi.org/10.1016/S0169-4332(02)00623-2.
(112) Den, W.; Bai, H.; Kang, Y. Organic Airborne Molecular Contamination in Semiconductor Fabrication Clean Rooms. *J. Electrochem. Soc.* **2006**, *153* (2), G149. https://doi.org/10.1149/1.2147286.
(113) Habuka, H.; Ishiwari, S.; Kato, H.; Shimada, M.; Okuyama, K. Airborne Organic Contamination Behavior on Silicon Wafer Surface. *J. Electrochem. Soc.* **2003**, *150* (2), G148. https://doi.org/10.1149/1.1536181.
(114) Xu, K.; Heath, J. R. Wetting: Contact with What? *Nat. Mater.* **2013**, *12* (10), 872–873. https://doi.org/10.1038/nmat3763.
(115) Patton, S. T.; Eapen, K. C.; Zabinski, J. S. Effects of Adsorbed Water and Sample Aging in Air on the MN Level Adhesion Force between Si(100) and Silicon Nitride. *Tribol. Int.* **2001**, *34* (7), 481–491. https://doi.org/10.1016/S0301-679X(01)00047-0.
(116) Rouxhet, P. G. Contact Angles and Surface Energy of Solids: Relevance and Limitations. *Advances in Contact Angle, Wettability and Adhesion*. July 16, 2013, pp 347–375. https://doi.org/10.1002/9781118795620.ch20.
(117) 3M. *Hydrophilicity and Surface Energy, a Little of the Science behind the Test Strip.*; 2018.
(118) Lipták, B. G.; Jamison, J. E.; Edvi, S. M. Pressure Gauges. *Instrument Engineers' Handbook: Process Measurement and Analysis, Fourth Edition*. June 20, 2003, pp 779–784. https://doi.org/10.1038/scientificamerican1101-29a.
(119) Booth, B. D.; Vilt, S. G.; Lewis, J. Ben; Rivera, J. L.; Buehler, E. A.; McCabe, C.; Jennings, G. K. Tribological Durability of Silane Monolayers on Silicon. *Langmuir* **2011**, *27* (10), 5909–5917. https://doi.org/10.1021/la104778q.
(120) Yang, Y.; Bittner, A. M.; Baldelli, S.; Kern, K. Study of Self-Assembled Triethoxysilane Thin Films Made by Casting Neat Reagents in Ambient Atmosphere. *Thin Solid Films* **2008**, *516* (12), 3948–3956. https://doi.org/10.1016/j.tsf.2007.07.208.
(121) Stevens, M. J. Thoughts on the Structure of Alkylsilane Monolayers. *Langmuir* **1999**, *15* (8), 2773–2778. https://doi.org/10.1021/la981064e.
(122) Yu, Y.; Krishnan, N. M. A.; Smedskjaer, M. M.; Sant, G.; Bauchy, M. The Hydrophilic-to-Hydrophobic Transition in Glassy Silica Is Driven by the Atomic Topology of Its Surface. *J. Chem. Phys.* **2018**, *148* (7), 74503. https://doi.org/10.1063/1.5010934.
(123) Rimsza, J. M.; Jones, R. E.; Criscenti, L. J. Surface Structure and Stability of Partially Hydroxylated Silica Surfaces. *Langmuir* **2017**, *33* (15), 3882–3891. https://doi.org/10.1021/acs.langmuir.7b00041.
(124) Yanazawa, H.; Matsuzawa, T.; Hashimoto, N. Evaluation of Hydrophobic SiO2 Surfaces Prepared by Fluorinated Organosilane Treatments. *J. Adhes. Sci. Technol.* **1990**, *4* (1), 145–153. https://doi.org/10.1163/156856190X00162.
(125) Cui, Y.; Wei, Q.; Park, H.; Lieber, C. M. Nanowire Nanosensors for Highly Sensitive and Selective Detection of Biological and Chemical Species. *Science (80-.).* **2001**, *293* (5533), 1289–1292. https://doi.org/10.1126/science.1062711.
(126) Wilson, N. R.; Pandey, P. A.; Beanland, R.; Rourke, J. P.; Lupo, U.; Rowlands, G.; Römer, R. A. On the Structure and Topography of Free-Standing Chemically Modified Graphene. *New J. Phys.* **2010**, *12* (12), 125010. https://doi.org/10.1088/1367-2630/12/12/125010.
(127) Palasantzas, G.; Krim, J. Effect of the Form of the Height-Height Correlation Function on Diffuse x-Ray Scattering from a Self-Affine Surface. *Phys. Rev. B* **1993**, *48* (5), 2873–2877. https://doi.org/10.1103/PhysRevB.48.2873.
(128) Amirzada, M. R.; Tatzel, A.; Viereck, V.; Hillmer, H. Surface Roughness Analysis of SiO2 for PECVD, PVD and IBD on Different Substrates. *Appl. Nanosci.* **2016**, *6* (2), 215–222. https://doi.org/10.1007/s13204-015-0432-8.
(129) Krim, J.; Indekeu, J. O. Roughness Exponents: A Paradox Resolved. *Phys. Rev. E* **1993**, *48* (2), 1576–1578. https://doi.org/10.1103/PhysRevE.48.1576.
(130) Saupe, D. Algorithms for Random Fractals. In *The Science of Fractal Images*; Barnsley, M. F., Devaney, R. L., Mandelbrot, B. B., Peitgen, H.-O., Saupe, D., Voss, R. F., Peitgen, H.-O., Saupe, D., Eds.; Springer New York: New York, NY, 1988; pp 71–136. https://doi.org/10.1007/978-1-4612-3784-6_2.
(131) Quéré, D. Wetting and Roughness. *Annu. Rev. Mater. Res.* **2008**, *38* (1), 71–99. https://doi.org/10.1146/annurev.matsci.38.060407.132434.
(132) Meshkova, A. S.; Starostin, S. A.; Van De Sanden, M. C. M.; De Vries, H. W. Variable Roughness Development in Statically Deposited SiO2 Thin Films: A Spatially Resolved Surface Morphology Analysis. *J. Phys. D. Appl. Phys.* **2018**, *51* (28), 285303. https://doi.org/10.1088/1361-6463/aacb1c.
(133) KRIM, J.; PALASANTZAS, G. EXPERIMENTAL OBSERVATIONS OF SELF-AFFINE SCALING AND KINETIC ROUGHENING AT SUB-MICRON LENGTHSCALES. *Int. J. Mod. Phys. B* **1995**, *09* (06), 599–632. https://doi.org/10.1142/S0217979295000239.
(134) Packham, D. E. Surface Energy, Surface Topography and Adhesion. *Int. J. Adhes. Adhes.* **2003**, *23* (6), 437–448. https://doi.org/10.1016/S0143-7496(03)00068-X.
(135) Bodner, T.; Behrendt, A.; Prax, E.; Wiesbrock, F. Correlation of Surface Roughness and Surface Energy of Silicon-Based Materials with Their Priming Reactivity. *Monatshefte fur Chemie* **2012**, *143* (5), 717–722. https://doi.org/10.1007/s00706-012-0730-8.
(136) Choi, K.; Ghosh, S.; Lim, J.; Lee, C. M. Removal Efficiency of Organic Contaminants on Si Wafer by Dry Cleaning Using UV/O 3 and ECR Plasma. *Appl. Surf. Sci.* **2003**, *206* (1–4), 355–364. https://doi.org/10.1016/S0169-4332(02)01215-1.
(137) Kolanek, K.; Tallarida, M.; Schmeisser, D. Height Distribution of Atomic Force Microscopy Images as a Tool for Atomic Layer Deposition Characterization. *J. Vac. Sci. Technol. A* **2012**, *31* (1), 01A104. https://doi.org/10.1116/1.4754557.
(138) Kolanek, K.; Tallarida, M.; Karavaev, K.; Schmeisser, D. In Situ Studies of the Atomic Layer Deposition of Thin HfO2 Dielectrics by Ultra High Vacuum Atomic Force Microscope. *Thin Solid Films* **2010**, *518* (16), 4688–4691. https://doi.org/10.1016/j.tsf.2009.12.060.
(139) Disrattakit, P.; Chanphana, R.; Chatraphorn, P. Skewness and Kurtosis of Height Distribution of Thin Films Simulated by Larger Curvature Model with Noise Reduction Techniques. *Phys. A Stat. Mech. its Appl.* **2017**, *484*, 299–308. https://doi.org/10.1016/j.physa.2017.04.075.
(140) Henrion, W.; Rebien, M.; Angermann, H.; Röseler, A. Spectroscopic Investigations of Hydrogen Termination, Oxide Coverage, Roughness, and Surface State Density of Silicon during Native Oxidation in Air. *Appl. Surf. Sci.* **2002**, *202* (3–4), 199–205. https://doi.org/10.1016/S0169-4332(02)00923-6.
(141) Hattori, T. Chemical Structures of the Sio2/Si Interface. *Crit. Rev. Solid State Mater. Sci.* **1995**, *20* (4), 339–382. https://doi.org/10.1080/10408439508240718.
(142) Azzam, R. M. A. *R. M. A. Azzam, and N. M. Bashara, Ellipsometry and Polarized Light (North-Holland, Amsterdam, 1994).*; Bashara, N. M., Ed.; North-Holland Pub. Co. ; sole distributors for the U.S.A. and Canada, Elsevier North-Holland: Amsterdam ; New York : New York, 1977.
(143) Bohling, C.; Sigmund, W. Self-Limitation of Native Oxides Explained. *Silicon* **2016**, *8* (3), 339–343. https://doi.org/10.1007/s12633-015-9366-8.
(144) Bohling, C.; Sigmund, W. Repulsive Van Der Waals Forces Self-Limit Native Oxide Growth. *Langmuir* **2015**, *31* (17), 4862–4867. https://doi.org/10.1021/acs.langmuir.5b00251.
(145) Chen, L.; Ngo, D.; Luo, J.; Gong, Y.; Xiao, C.; He, X.; Yu, B.; Qian, L.; Kim, S. H. Dependence of Water Adsorption on the Surface Structure of Silicon Wafers Aged under Different Environmental Conditions. *Phys. Chem. Chem. Phys.* **2019**, *21* (47), 26041–26048. https://doi.org/10.1039/c9cp04776j.
(146) Kanyal, S. S.; Jensen, D. S.; Zhu, Z.; Linford, M. R. Silicon (100)/SiO2 by ToF-SIMS. *Surf. Sci. Spectra* **2015**, *22* (2), 1–6. https://doi.org/10.1116/1.4930256.
(147) Stingeder, G.; Grundner, M.; Grasserbauer, M. Investigation of Surface Contamination on Silicon Wafers with SIMS. *Surf. Interface Anal.* **1988**, *11* (8), 407–413. https://doi.org/10.1002/sia.740110802.

(148) Hattori, T. Chemical Contamination Control in ULSI Wafer Processing. *AIP Conf. Proc.* **2003**, *550* (1), 275–284. https://doi.org/10.1063/1.1354411.

(149) Licciardello, A.; Puglisi, O.; Pignataro, S. Effect of Organic Contaminants on the Oxidation Kinetics of Silicon at Room Temperature. *Appl. Phys. Lett.* **1986**, *48* (1), 41–43. https://doi.org/10.1063/1.96755.

(150) Barabási, A.-L.; Stanley, H. E. *Fractal Concepts in Surface Growth*; Cambridge University Press: Cambridge [u.a.], 2002.

(151) Seah, M. P.; Spencer, S. J. Ultrathin SiO2 on Si IV. Intensity Measurement in XPS and Deduced Thickness Linearity. *Surf. Interface Anal.* **2003**, *35* (6), 515–524. https://doi.org/10.1002/sia.1565.

(152) Oh, J. H.; Yeom, H. W.; Hagimoto, Y.; Ono, K.; Oshima, M.; Hirashita, N.; Nywa, M.; Toriumi, A.; Kakizaki, A. Chemical Structure of the Ultrathin SiO2/Si(100) Interface:An Angle-Resolved Si 2p Photoemission Study. *Phys. Rev. B - Condens. Matter Mater. Phys.* **2001**, *63* (20), 205310. https://doi.org/10.1103/PhysRevB.63.205310.

(153) Himpsel, F. J.; McFeely, F. R.; Taleb-Ibrahimi, A.; Yarmoff, J. A.; Hollinger, G. Microscopic Structure of the SiO2/Si Interface. *Phys. Rev. B* **1988**, *38* (9), 6084–6096. https://doi.org/10.1103/PhysRevB.38.6084.

(154) Bongiorno, A.; Pasquarello, A. Atomistic Model Structure of the Si(1 0 0)-SiO 2 Interface from a Synthesis of Experimental Data. *Appl. Surf. Sci.* **2004**, *234* (1–4), 190–196. https://doi.org/10.1016/j.apsusc.2004.05.020.

(155) Li, P.; Chen, Z.; Yao, P.; Zhang, F.; Wang, J.; Song, Y.; Zuo, X. First-Principles Study of Defects in Amorphous-SiO 2 /Si Interfaces. *Appl. Surf. Sci.* **2019**, *483*, 231–240. https://doi.org/10.1016/j.apsusc.2019.03.216.

(156) De La Peña, F.; Barrett, N.; Zagonel, L. F.; Walls, M.; Renault, O. Full Field Chemical Imaging of Buried Native Sub-Oxide Layers on Doped Silicon Patterns. *Surf. Sci.* **2010**, *604* (19–20), 1628–1636. https://doi.org/10.1016/j.susc.2010.06.006.

(157) Jones, D.; Palermo, V. Production of Nanostructures of Silicon on Silicon by Atomic Self-Organization Observed by Scanning Tunneling Microscopy. *Appl. Phys. Lett.* **2002**, *80* (4), 673–675. https://doi.org/10.1063/1.1445813.

(158) Seah, M. P. Intercomparison of Silicon Dioxide Thickness Measurements Made by Multiple Techniques: The Route to Accuracy. *J. Vac. Sci. Technol. A Vacuum, Surfaces, Film.* **2004**, *22* (4), 1564–1571. https://doi.org/10.1116/1.1705594.

(159) Baikie, I. D.; Petermann, U.; Speakman, A.; Lägel, B.; Dirscherl, K. M.; Estrup, P. J. Work Function Study of Rhenium Oxidation Using an Ultra High Vacuum Scanning Kelvin Probe. *J. Appl. Phys.* **2000**, *88* (7), 4371–4375. https://doi.org/10.1063/1.1289486.

(160) Li, P.; Appelbaum, I. *Electrons and Holes in Phosphorene*; Prentice Hall Upper Saddle River, NJ, 2014; Vol. 90. https://doi.org/10.1103/PhysRevB.90.115439.

(161) Shao, G. Work Function and Electron Affinity of Semiconductors: Doping Effect and Complication Due to Fermi Level Pinning. *Energy Environ. Mater.* **2021**, *4* (3), 273–276. https://doi.org/10.1002/eem2.12218.

(162) Sze, S. M.; Ng, K. K. Physics and Properties of Semiconductors-A Review. *Physics of Semiconductor Devices*. October 13, 2006, pp 5–75. https://doi.org/10.1002/9780470068328.ch1.

(163) Mizsei, J. Fermi-Level Pinning and Passivation on the Oxide-Covered and Bare Silicon Surfaces and Interfaces. *Vacuum* **2002**, *67* (1), 59–67. https://doi.org/10.1016/S0042-207X(02)00200-2.

(164) Sze, S. M.; Ng, K. K. Metal-Insulator-Semiconductor Capacitors. In *Physics of Semiconductor Devices*; John Wiley & Sons, Ltd, 2006; pp 197–240. https://doi.org/10.1002/9780470068328.ch4.

(165) Cowley, A. M.; Sze, S. M. Surface States and Barrier Height of Metal-Semiconductor Systems. *J. Appl. Phys.* **1965**, *36* (10), 3212–3220. https://doi.org/10.1063/1.1702952.

(166) Hirose, K.; Nohira, H.; Azuma, K.; Hattori, T. Photoelectron Spectroscopy Studies of SiO2/Si Interfaces. *Prog. Surf. Sci.* **2007**, *82* (1), 3–54. https://doi.org/10.1016/j.progsurf.2006.10.001.

(167) Khalilov, U.; Neyts, E. C.; Pourtois, G.; Van Duin, A. C. T. Can We Control the Thickness of Ultrathin Silica Layers by Hyperthermal Silicon Oxidation at Room Temperature? *J. Phys. Chem. C* **2011**, *115* (50), 24839–24848. https://doi.org/10.1021/jp2082566.

(168) Schroder, D. K. Surface Voltage and Surface Photovoltage: History, Theory and Applications. *Meas. Sci. Technol.* **2001**, *12* (3), 16–31. https://doi.org/10.1088/0957-0233/12/3/202.

(169) Statz, H.; DeMars, G. A.; Davis, L.; Adams, A. Surface States on Silicon and Germanium Surfaces. *Phys. Rev.* **1956**, *101* (4), 1272–1281. https://doi.org/10.1103/PhysRev.101.1272.

(170) Sze, S. M. Metal-Semiconductor Contacts. *Physics of Semiconductor Devices*. October 13, 2006, pp 134–196. https://doi.org/https://doi.org/10.1002/9780470068328.ch3.

(171) Tuft, R. A. Bandgap Narrowing in Moderately to Heavily Doped Silcon. *IEEE Trans. Electron Devices* **1979**, *26* (7), 1014–1018. https://doi.org/10.1109/T-ED.1979.19538.

(172) Bonilla, R. S. Modelling of Kelvin Probe Surface Voltage and Photovoltage in Dielectric-Semiconductor Interfaces. *Mater. Res. Express* **2022**, *9* (8), 85901. https://doi.org/10.1088/2053-1591/ac84c8.

(173) Dalstein, L.; Potapova, E.; Tyrode, E. The Elusive Silica/Water Interface: Isolated Silanols under Water as Revealed by Vibrational Sum Frequency Spectroscopy. *Phys. Chem. Chem. Phys.* **2017**, *19* (16), 10343–10349. https://doi.org/10.1039/c7cp01507k.

(174) You, Y.; Chen, J.; Zheng, A.; Wei, D.; Xu, X.; Guan, Y. Effect of Silanol on the Thermal Stability of Poly[Methyl(Trifluoropropyl)Siloxane]. *J. Appl. Polym. Sci.* **2020**, *137* (44), 49347. https://doi.org/10.1002/app.49347.

(175) Podolian, A.; Nadtochiy, A.; Kuryliuk, V.; Korotchenkov, O.; Schmid, J.; Drapalik, M.; Schlosser, V. The Potential of Sonicated Water in the Cleaning Processes of Silicon Wafers. *Sol. Energy Mater. Sol. Cells* **2011**, *95* (2), 765–772. https://doi.org/10.1016/j.solmat.2010.10.019.

(176) Shimizu, H.; Munakata, C. Nondestructive Characterization of Surface Contaminants in Silicon Wafers Using AC Surface Photo Voltage Method. *Mater. Trans. Jim* **1994**, *35* (11), 827–832. https://doi.org/10.2320/matertrans1989.35.827.

(177) Girisch, R. B. M.; Mertens, R. P.; De Keersmaecker, R. F. Determination of Si-SiO2 Interface Recombination Parameters Using a Gate-Controlled Point-Junction Diode Under Illumination. *IEEE Trans. Electron Devices* **1988**, *35* (2), 203–222. https://doi.org/10.1109/16.2441.

(178) Albonetti, C.; Chiodini, S.; Annibale, P.; Stoliar, P.; Martinez, R. V.; Garcia, R.; Biscarini, F. Quantitative Phase-Mode Electrostatic Force Microscopy on Silicon Oxide Nanostructures. *J. Microsc.* **2020**, *280* (3), 252–269. https://doi.org/10.1111/jmi.12938.

(179) Landsberg, P. T.; Kousik, G. S. The Connection between Carrier Lifetime and Doping Density in Nondegenerate Semiconductors. *J. Appl. Phys.* **1984**, *56* (6), 1696–1700. https://doi.org/10.1063/1.334159.

(180) Philipossian, A. The Activity of HF / H 2 O Treated Silicon Surfaces in Ambient Air Before and After Gate Oxidation. *J. Electrochem. Soc.* **1992**, *139* (10), 2956–2961. https://doi.org/10.1149/1.2069015.

(181) Sze, S. M.; Ng, K. K. P - n Junctions . *Physics of Semiconductor Devices*. October 13, 2006, pp 77–133. https://doi.org/10.1002/9780470068328.ch2.

(182) Chemla, M.; Bertagna, V.; Rouelle, F.; Petitdidier, S.; Levy, D. Semiconductor Space Charge and Surface Oxide Thin Layers Capacitance by Electrochemical Impedance Spectroscopy. *Electrochemistry* **2003**, *71* (10), 844–852. https://doi.org/10.5796/electrochemistry.71.844.

(183) Okorn-Schmidt, H. F. Characterization of Silicon Surface Preparation Processes for Advanced Gate Dielectrics. *IBM J. Res. Dev.* **1999**, *43* (3), 351–365. https://doi.org/10.1147/rd.433.0351.

(184) Saga, K.; Kuniyasu, H.; Hattori, T. Influence of Ambient Oxygen and Moisture on the Growth of Native Oxides on Silicon Surfaces. *Test. Electrochem.* **1999**, *1*, 1–3.

(185) Gräf, D.; Grundner, M.; Schulz, R.; Mühlhoff, L. Oxidation of HF-

Treated Si Wafer Surfaces in Air. *J. Appl. Phys.* **1990**, *68* (10), 5155–5161. https://doi.org/10.1063/1.347056.

(186) Gibbs, G. V.; Cox, D. F.; Boisen, J. B.; Downs, R. T.; Ross, N. L. The Electron Localization Function: A Tool for Locating Favorable Proton Docking Sites in the Silica Polymorphs. *Phys. Chem. Miner.* **2003**, *30* (5), 305–316. https://doi.org/10.1007/s00269-003-0318-2.

(187) Hillborg, H.; Gedde, U. W. Hydrophobicity Changes in Silicone Rubbers. *IEEE Trans. Dielectr. Electr. Insul.* **2020**, *6* (5), 703–717. https://doi.org/10.1109/tdei.1999.9286748.

(188) Bhattacharya, S.; Datta, A.; Berg, J. M.; Gangopadhyay, S. Studies on Surface Wettability of Poly(Dimethyl) Siloxane (PDMS) and Glass under Oxygen-Plasma Treatment and Correlation with Bond Strength. *J. Microelectromechanical Syst.* **2005**, *14* (3), 590–597. https://doi.org/10.1109/JMEMS.2005.844746.

(189) Stallard, C. P.; McDonnell, K. A.; Onayemi, O. D.; O'Gara, J. P.; Dowling, D. P. Evaluation of Protein Adsorption on Atmospheric Plasma Deposited Coatings Exhibiting Superhydrophilic to Superhydrophobic Properties. *Biointerphases* **2012**, *7* (1–4), 1–12. https://doi.org/10.1007/s13758-012-0031-0.

(190) Rückriem, M.; Inayat, A.; Enke, D.; Gläser, R.; Einicke, W. D.; Rockmann, R. Inverse Gas Chromatography for Determining the Dispersive Surface Energy of Porous Silica. *Colloids Surfaces A Physicochem. Eng. Asp.* **2010**, *357* (1–3), 21–26. https://doi.org/10.1016/j.colsurfa.2009.12.001.

(191) Ligner, G.; Vidal, A.; Balard, H.; Papirer, E. London Component of the Surface Energy of Heat-Treated Silicas. *J. Colloid Interface Sci.* **1989**, *133* (1), 200–210. https://doi.org/10.1016/0021-9797(89)90293-2.

(192) Bormashenko, E. Physics of Solid-Liquid Interfaces: From the Young Equation to the Superhydrophobicity (Review Article). *Low Temp. Phys.* **2016**, *42* (8), 622–635. https://doi.org/10.1063/1.4960495.

(193) Roscioni, O. M. Materialx: Molecular Modelling As A Service https://materialx.co.uk/.

(194) Godin, K.; Kang, K.; Fu, S.; Yang, E. H. Increased Monolayer Domain Size and Patterned Growth of Tungsten Disulfide through Controlling Surface Energy of Substrates. *J. Phys. D. Appl. Phys.* **2016**, *49* (32), 325304. https://doi.org/10.1088/0022-3727/49/32/325304.

(195) Williams, R.; Goodman, A. M. Wetting of Thin Layers of SiO2 by Water. *Appl. Phys. Lett.* **1974**, *25* (10), 531–532. https://doi.org/10.1063/1.1655297.

(196) Seah, M. P.; Spencer, S. J. Ultrathin SiO2 on Si II. Issues in Quantification of the Oxide Thickness. *Surf. Interface Anal.* **2002**, *33* (8), 640–652. https://doi.org/10.1002/sia.1433.

(197) Ishimaru, Y.; Yoshiki, M.; Hatanaka, T. The Effect of Dopant Concentration on the Native Oxide Growth on Silicon Wafer Surface. *MRS Proc.* **1992**, *259* (1), 405–408. https://doi.org/10.1557/proc-259-405.

(198) Kandilioti, G.; Siokou, A.; Papaefthimiou, V.; Kennou, S.; Gregoriou, V. G. Molecular Composition and Orientation of Interstitial versus Surface Silicon Oxides for Si(111)/SiO2 and Si(100)/SiO2 Interfaces Using FT-IR and X-Ray Photoelectron Spectroscopies. *Appl. Spectrosc.* **2003**, *57* (6), 628–635. https://doi.org/10.1366/000370203322005300.

(199) Grundner, M.; Jacob, H. Investigations on Hydrophilic and Hydrophobic Silicon (100) Wafer Surfaces by X-Ray Photoelectron and High-Resolution Electron Energy Loss-Spectroscopy. *Appl. Phys. A Solids Surfaces* **1986**, *39* (2), 73–82. https://doi.org/10.1007/BF00616822.

(200) Aoyama, T.; Yamazaki, T.; Ito, T. Removing Native Oxide from Si(001) Surfaces Using Photoexcited Fluorine Gas. *Appl. Phys. Lett.* **1991**, *59* (20), 2576–2578. https://doi.org/10.1063/1.105930.

(201) Mazur, J. H.; Gronsky, R.; Washburn, J. High Resolution Electron Microscopy Studies of Native Oxide on Silicon. In *Institute of Physics Conference Series*; CRC Press, 1983; pp 77–82. https://doi.org/10.1201/9781003069614-12.

(202) Carim, A. H.; Dovek, M. M.; Quate, C. F.; Sinclair, R.; Vorst, C. High-Resolution Electron Microscopy and Scanning Tunneling Microscopy of Native Oxides on Silicon. *Science (80-.).* **1987**, *237* (4815), 630–633. https://doi.org/10.1126/science.237.4815.630.

(203) Ishigami, S. I.; Kondoh, H.; Ryuta, J.; Kawai, Y.; Furuya, H. Effect of Native Oxide upon Formation of Amorphous SiOx Layer at the Interface of Directly Bonded Silicon Wafers. *Jpn. J. Appl. Phys.* **1995**, *34* (2R), 425–429. https://doi.org/10.1143/JJAP.34.425.

(204) Grovenora, C. R. M.; Cerezo, A.; Smith, G. D. W. Atom Probe Analysis of Native Oxides and the Thermal Oxide/Silicon Interface. *MRS Proc.* **1984**, *37* (1), 199–204. https://doi.org/10.1557/proc-37-199.

(205) Philipp, H. R.; Taft, E. A. An Optical Characterization of Native Oxides and Thin Thermal Oxides on Silicon. *J. Appl. Phys.* **1982**, *53* (7), 5224–5229. https://doi.org/10.1063/1.331401.

(206) Ewing, G. E. Ambient Thin Film Water on Insulator Surfaces. *Chem. Rev.* **2006**, *106* (4), 1511–1526. https://doi.org/10.1021/cr040369x.

(207) A Picard; H Fang. Methods to Determine Water Vapour Sorption on Mass Standards. *Metrologia* **2004**, *41* (4), 333. https://doi.org/10.1088/0026-1394/41/4/016.

(208) Thiel, P. A.; Madey, T. E. The Interaction of Water with Solid Surfaces: Fundamental Aspects. *Surf. Sci. Rep.* **1987**, *7* (6), 211–385. https://doi.org/https://doi.org/10.1016/0167-5729(87)90001-X.

(209) Quinn, A.; Sedev, R.; Ralston, J. Contact Angle Saturation in Electrowetting. *J. Phys. Chem. B* **2005**, *109* (13), 6268–6275. https://doi.org/10.1021/jp040478f.

(210) Quilliet, C.; Berge, B. Electrowetting: A Recent Outbreak. *Curr. Opin. Colloid Interface Sci.* **2001**, *6* (1), 34–39. https://doi.org/10.1016/S1359-0294(00)00085-6.

(211) Stoneham, A. M.; Tasker, P. W. Metal-Non-Metal and Other Interfaces: The Role of Image Interactions. *J. Phys. C Solid State Phys.* **1985**, *18* (19), L543–L548. https://doi.org/10.1088/0022-3719/18/19/001.

(212) Hase, T. Tables for organic spectrometry http://www.stenutz.eu/chem/.

(213) Wolkenberg, A.; Wasilewska, B. Properties of Boron Implanted Silicon Dioxide. *Appl. Surf. Sci.* **1979**, *3* (1), 83–87. https://doi.org/10.1016/0378-5963(79)90062-X.

(214) Sigmon, T. W.; Chu, W. K.; Lugujjo, E.; Mayer, J. W. Stoichiometry of Thin Silicon Oxide Layers on Silicon. *Appl. Phys. Lett.* **1974**, *24* (3), 105–107. https://doi.org/10.1063/1.1655112.

(215) Morita, M.; Ohmi, T. Characterization and Control of Native Oxide on Silicon. *Jpn. J. Appl. Phys.* **1994**, *33* (1), 370–374. https://doi.org/10.1143/JJAP.33.370.

(216) Kovalgin, A. Y.; Zinine, A.; Bankras, R.; Wormeester, H.; Poelsema, B.; Schmitz, J. On the Growth of Native Oxides on Hydrogen-Terminated Silicon Surfaces in Dark and Under Illumination with Light. *ECS Trans.* **2006**, *3* (2), 191–202. https://doi.org/10.1149/1.2356279.

(217) Dinelli, F.; Albonetti, C.; Kolosov, O. V. Ultrasonic Force Microscopy: Detection and Imaging of Ultra-Thin Molecular Domains. *Ultramicroscopy* **2011**, *111* (4), 267–272. https://doi.org/10.1016/j.ultramic.2010.12.019.

(218) Chiodini, S.; D'Avino, G.; Muccioli, L.; Bartolini, L.; Gentili, D.; Toffanin, S.; Albonetti, C. Self-Organization of Complete Organic Monolayers via Sequential Post-Deposition Annealing. *Prog. Org. Coatings* **2020**, *138*. https://doi.org/10.1016/j.porgcoat.2019.105408.

(219) Yao, J.; Zhong, L.; Natelson, D.; Tour, J. M. Silicon Oxide: A Non-Innocent Surface for Molecular Electronics and Nanoelectronics Studies. *J. Am. Chem. Soc.* **2011**, *133* (4), 941–948. https://doi.org/10.1021/ja108277r.

(220) Evans, J. W.; Thiel, P. A.; Bartelt, M. C. Morphological Evolution during Epitaxial Thin Film Growth: Formation of 2D Islands and 3D Mounds. *Surf. Sci. Rep.* **2006**, *61* (1–2), 1–128. https://doi.org/https://doi.org/10.1016/j.surfrep.2005.08.004.

(221) Pratontep, S.; Nüesch, F.; Zuppiroli, L.; Brinkmann, M. Comparison between Nucleation of Pentacene Monolayer Islands on Polymeric and Inorganic Substrates. *Phys. Rev. B* **2005**, *72* (8), 85211.

https://doi.org/10.1103/PhysRevB.72.085211.

(222) Chiodini, S.; Stoliar, P.; Garrido, P. F.; Albonetti, C. Differential Entropy: An Appropriate Analysis to Interpret the Shape Complexity of Self-Similar Organic Islands. *Materials*. 2021. https://doi.org/10.3390/ma14216529.

(223) Nečas, D.; Klapetek, P. Gwyddion: An Open-Source Software for SPM Data Analysis. *Cent. Eur. J. Phys.* **2012**, *10* (1), 181–188. https://doi.org/10.2478/s11534-011-0096-2.